Nordbäck *et al. Geothermal Energy* (2026) 14:1
https://doi.org/10.1186/s40517-025-00370-5

Geothermal Energy

RESEARCH **Open Access**

Strike-slip faulting and hydrothermal alteration in a Proterozoic rapakivi batholith: implications for reservoir formation and geothermal exploration in crystalline cratons—Part 1

Nicklas Nordbäck[1*], Alan Bischoff[2], Daniel Carbajal-Martinez[1], Jon Engström[1], Kaisa Nikkilä[3], Pietari Skyttä[4], Andrew Nicol[5], Nikolas Ovaskainen[1] and Steffi Burchardt[6,7]

*Correspondence:
nicklas.nordback@gtk.fi

[1] Geological Survey of Finland, Espoo, Finland
[2] University of Turku, Turku, Finland
[3] Åbo Akademi University, Turku, Finland
[4] Structural Geology Company, Turku, Finland
[5] University of Canterbury, Christchurch, New Zealand
[6] Department of Earth Sciences, Uppsala University, Uppsala, Sweden
[7] Centre of Natural Hazards and Disaster Science, Uppsala University, Uppsala, Sweden

Abstract

Ancient crystalline basement cratons are traditionally considered challenging geothermal targets due to their low heat flow, limited porosity, and low matrix permeability. However, fractured and hydrothermally altered crystalline basement rocks can exhibit substantial permeability and fluid storage capacity, making them viable unconventional geothermal prospects. This study examines the brittle deformation processes of the Vehmaa Batholith, a Proterozoic rapakivi intrusion emplaced in Southern Finland, and has implications for geothermal exploration in stable cratonic regions. It evaluates the batholith's potential to host kilometer-scale geothermal reservoirs and offers insights for exploring geothermal resources in crystalline rocks affected by faulting and hydrothermal alteration. Detailed structural mapping, drone photogrammetry, remote sensing, and paleostress analysis reveal two principal ENE–WSW and NNW–SSE strike-slip fault systems transecting the batholith, interpreted to result from distinct Mesoproterozoic tectonic events. These faults generated extensive fracture networks that align with regional lineaments traceable for ~10–25 km, with scaling relationships indicating damage zones ~100–250 m wide. These fracture networks also exhibit high connectivity, with topological relationship values well exceeding the threshold for continuous fluid pathways, and are typically associated with intense hydrothermal alteration, including chloritization, sericitization, and dissolution-related porosity. The spatial association between brittle structures and hydrothermal alteration supports a model where fluid circulation is controlled by post-magmatic faults, which significantly enhance reservoir properties in crystalline rocks. This has direct implications for geothermal exploration in cratonic regions, where such structures may compensate for otherwise poor hydraulic conditions and enhance advective heat flow. Based on structural criteria, we define five major fault-controlled geothermal targets within the Vehmaa Batholith, representing new exploration opportunities in crystalline basement. Our findings provide the first systematic evidence of large-scale fracture connectivity and reservoir development in rapakivi granites and contribute to broader strategies for identifying geothermal resources in stable continental crust.

Keywords: Geothermal reservoirs, Fault zones, Hydrothermal alteration, Crystalline rocks, Fennoscandian Shield

Introduction

Precambrian crystalline basement cratons constitute extensive portions of the Earth's crust. They are characterized by low heat flow and very low rock-permeability, which pose significant challenges for geothermal exploration (Jolie et al. 2021; Kukkonen et al. 2023). Nevertheless, faults and hydrothermal alteration can create fluid pathways that enable circulation within the otherwise low-permeability crystalline basement, increasing advective heat flow and making these regions viable unconventional geothermal targets (Sausse and Genter 2005; Caspari et al. 2020; Kraal et al. 2021; Berger and Herwegh 2022; Bischoff et al. 2024; Harpers et al. 2024). Such viable geothermal systems have been documented in multiple locations, including the Canadian Rocky Mountains (Grasby and Hutcheon 2001), the Nepalese Himalaya (Whipp and Ehlers 2007), the Da Qaidam Basin in China (Stober et al. 2016), the Swiss Alps (Diamond et al. 2018), the French Pyrenees (Taillefer et al. 2018), the Basin and Range province in western USA (Siler et al. 2019), and parts of Baja California, Mexico (Carbajal-Martínez et al. 2024), where faults often enhance permeability, allowing fluids to reach significant depths and form geothermal reservoirs. However, in ancient crystalline settings not experiencing contemporary tectonic deformation, outcomes are often modest, as faults do not always provide sufficient permeability to support commercially viable geothermal systems and, in some cases, the low hydraulic conductivity of crystalline rocks has led to the closure of geothermal projects (Kukkonen et al. 2023).

Despite this inherent thermo-hydraulic challenge of old cratonic regions, the exploration of geothermal resources has already grown into a multi-million-euro market in areas of crystalline basement, such as the Fennoscandian Shield (Arola and Wiberg 2022; Sanner et al. 2022). Unlike the generation of electricity, geothermal heating and cooling applications rely on much lower working temperatures, enabling technologies such as ground-source heat pumps, heat exchangers, and borehole fields to make an impactful contribution to global energy markets. Currently, shallow (<1 km), low-temperature (<150 °C) resources are estimated to supply about half of all geothermal heat consumed globally, with nearly 10 $\mathrm{GW_{th}}$ installed capacity in the Fennoscandian Shield alone (IRENA 2022; IEA 2024). As technology advances, it creates significant potential for expanding exploratory frontiers, particularly in the development of cost-competitive geothermal systems in deeper (>1 km) crystalline settings.

The notable contrasting outcomes of geothermal projects in crystalline settings highlight the need to better understand the mechanisms that govern permeability within faults in these ancient cratonic areas, where present-day tectonic activity is minimal. Recent studies have begun addressing these challenges by, for example, (i) advancing our knowledge of the brittle tectonic evolution in central Fennoscandia (Skyttä et al. 2021; Nordbäck et al. 2022, 2024); (ii) increasing understanding of fracture topology and fault geometry at multiple scales (Nordbäck et al. 2023; Ovaskainen et al. 2023); and (iii) establishing the links between faulting and hydrothermal alteration (Bischoff et al. 2024).

Key unresolved questions are: How do faults and associated hydrothermal alteration control the formation and connectivity of large-scale crystalline reservoirs in ancient cratons? What are the key characteristics for identifying geothermal systems in such settings?.

Inspired by geothermal developments in the Rhine Graben (France) and Cornwall (UK), where faulted and altered crystalline reservoirs are exploited for fluid circulation and heat production (Genter et al. 2010; Glaas et al. 2021; Reinecker et al. 2021; Farndale and Law 2022), our study examines the role of faulting and hydrothermal alteration in forming large-scale geothermal reservoirs in Finland. This is the first in a series of two papers. Here, we present results from a multiscale analysis of brittle structures transecting the 1.57 Ga Vehmaa Rapakivi Batholith in southwestern Finland (Lindberg and Bergman 1993; Fig. 1). Complementary, investigations into mineral alterations and their effects on petrophysical and thermal variations in the Vehmaa rapakivi rocks will be presented in a second paper and are not considered in detail here.

Using a diverse dataset, including regional lineament mapping, unmanned aerial vehicle (UAV)-based photogrammetry, and field structural analysis of nearly 70 key locations across the Vehmaa Batholith, we investigate the formation, multiscale connectivity, dimensions, and extent of faults intersecting this rapakivi body. Our multiscale analysis provides critical insights for identifying possible fluid pathways and optimal targets for geothermal exploration in ancient crystalline settings, while also providing first-order estimations of heat production in low-enthalpy areas such as the Fennoscandian Shield.

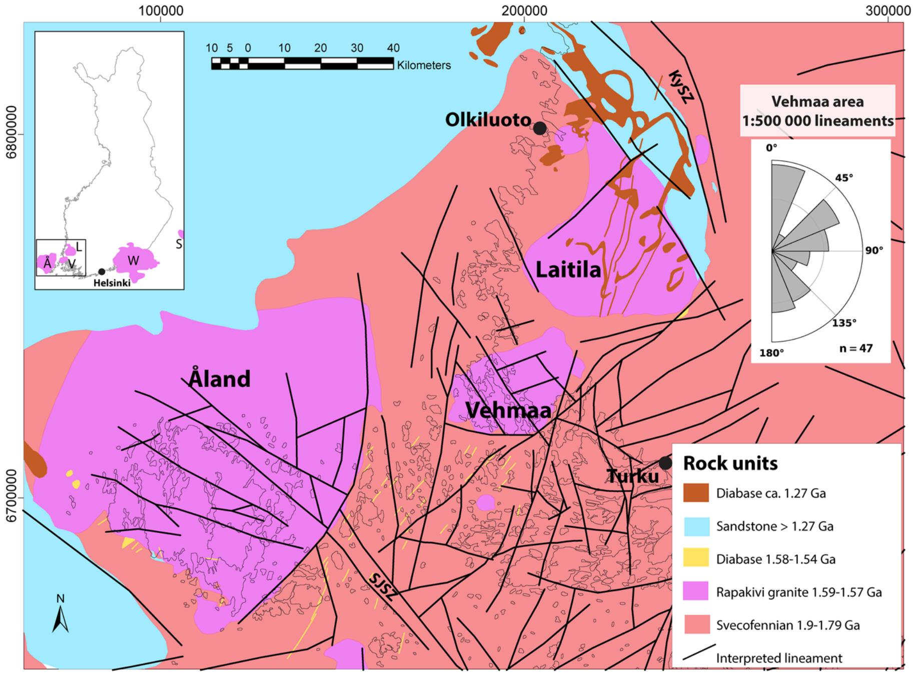

Fig. 1 Generalized geological map of SW Finland. The figure is based on the geological map of the Fennoscandian Shield 1:1,000,000 (GTK 2001). Lineaments are modified from Nordbäck et al. (2024). Rose plot displays the orientation of 1:500,000-scale lineaments within <30 km distance from the Vehmaa Batholith. *Å* Åland Batholith, *V* Vehmaa Batholith, *L* Laitila Batholith, *W* Wiborg Batholith, *S* Salmi Batholith, *SJSZ* Sottunga-Jurmo Shear Zone (Torvela and Ehlers 2010), *KySZ* Kynsikangas Shear Zone

Additionally, our new data and interpretations significantly advance the understanding of the tectonic and thermal evolution of the crystalline crust in southern Finland, particularly the timing, extent, and interplay of brittle deformation and hydrothermal alteration events, enriching the existing literature on crystalline reservoirs (Ledésert et al. 2010; Achtziger-Zupančič et al. 2017; Duwiquet et al. 2021; Frey et al. 2022). Ultimately, the insights gained from this study will support the development of numerical models to quantify fluid flow parameters in crystalline reservoirs while enabling the energy industry to assess how faults can form extensive geothermal targets, both in Finland and in similar cratonic settings worldwide.

Geological background

Tectono-structural setting

Southwestern Finland bedrock is dominated by Paleoproterozoic granites, migmatites, and supracrustal rocks that underwent ductile deformation and metamorphism during the Svecofennian orogeny at 1.9–1.8 Ga (Fig. 1; Nironen 1997; Lahtinen et al. 2009). Brittle deformation in southern Finland initiated between 1.79 and 1.72 Ga (Torvela et al. 2008; Marchesini et al. 2019; Prando et al. 2020) and involved reactivation of pre-existing Svecofennian ductile shear structures (Väisänen and Skyttä, 2007), as well as the formation of new brittle faults under NNW–SSE compression (Mattila and Viola 2014).

After this initial Paleoproterozoic compressional regime, southern Finland experienced multiple extensional phases associated with bimodal anorogenic magmatism and the emplacement of rapakivi granites between 1.64 and 1.57 Ga. North–South extension was dominant during the emplacement of the 1.64 Ga Wiborg Rapakivi Batholith (Fig. 1; Nironen 1997), followed by E–W to NW–SE extension at around 1.59–1.57 Ga (Nordbäck et al. 2024). Coeval with the later 1.59–1.57 Ga rapakivi magmatism, diabase dykes are reported across all southwestern Finland, all presumably related to E–W to NW–SE extension (Suominen 1991; Rämö and Haapala 1995). This magmatic activity generated large sheet-like batholithic intrusions and smaller plutons, including the Vehmaa (i.e., the object of this study), Åland, and Laitila rapakivi granites (Fig. 1). Crustal thinning during these stages initiate subsidence and the formation of an intracratonic sedimentary basin, currently located near the southwestern coast of Finland and beneath the Bothnian Sea (Korja et al. 1993). Sedimentary and igneous rocks deposited and emplaced during this stage are preserved onshore within the Satakunta Formation (Pokki et al. 2013) that was deposited into a fault-bounded basin north of the Laitila Rapakivi Batholith (Fig. 1), and the Satakunta diabase intrusions. The minimum age of the Satakunta formation is constrained by the intrusion of 1.27 Ga diabase dykes and sills (Suominen 1991), while the age of the oldest parts of the basin is estimated to range from 1.65 to 1.3 Ga (Simonen 1980; Kohonen et al. 1993; Pokki et al. 2013).

Detailed studies with regional coverage over the brittle structures in SW Finland have been spatially restricted to analysis of the Åland Rapakivi Batholith (Fig. 1), indicating two Mesoproterozoic strike-slip faulting stages: (i) the older 1.55–1.4 Ga WNW–ESE to NNW–SSE compression and (ii) the younger 1.3–1.2 Ga NE–SW compression (Nordbäck et al. 2024). The first stage is tentatively correlated with Mesoproterozoic extension and late-rapakivi magmatism, while the second stage is time-constrained by K–Ar isotopic data of fault reactivation at the Olkiluoto nuclear repository site (Nordbäck et al.

2022; Fig. 1), coinciding with the intrusion of the 1.27 Ga Satakunta diabase. This suggests that Mesoproterozoic tectonics in southwestern Finland may have involved local strike-slip faulting during regional crustal rifting.

The youngest fault system recorded in the crust of southwestern Finland consists of low-angle thrust faults, formed during the Sveconorwegian orogeny (ca. 1.1 Ga ago; Mattila and Viola 2014; Nordbäck et al. 2022). Joints are also often observed in Finnish rapakivi granites. Using crosscutting relationships between strike-slip faults and joints in the Åland Batholith, Nordbäck et al. (2024) estimated the maximum age of jointing at around 1.2 Ga, and the presence of sedimentary dykes emplaced within these joints (Bergman et al. 1982; Tynni 1982) further supports the interpretation that the joints predate Cambrian sedimentation. Following the Sveconorwegian orogeny, brittle deformation in southern Finland was largely limited to minor fault reactivations, and it is generally accepted that from around 900 million years ago, the region transitioned into a tectonically stable area (Mattila and Viola 2014; Green et al. 2022; Nordbäck et al. 2022). Evidence of later activity is sparse; some fault reactivation during the Caledonian orogeny (Late Cambrian to Early Devonian) has been identified from isotopically dated fault gouge samples in southeastern Sweden (Saintot et al. 2011) and southwestern Finland (Viola et al. 2011). Moreover, apatite fission-track thermochronology indicates that the region experienced significant cooling following tectonic quiescence after the Sveconorwegian orogeny, with only minor subsequent thermal perturbations throughout the Phanerozoic, as paleotemperatures are inferred to have reached approximately 60 ± 10 °C due to sedimentary burial (Kukkonen et al. 2025).

The present-day stress field in southern Finland is compressional (thrust), influenced by the spreading of the Mid-Atlantic Ridge. Available stress data come from the upper crust (depths < 1 km), with the dominant orientation of the maximum horizontal stress (σ_H) being NW–SE to E–W oriented (Heidbach et al. 2025). In central Fennoscandia, where post-glacial rebound is most pronounced, the strain field is, however, dominated by extensional deformation, with rates reaching up to 5 nanostrain per year (Scherneck et al. 2010). According to the seismic catalogue (Uski et al. 2025), the seismicity in southwestern Finland is low.

Vehmaa rapakivi batholith

Rapakivi batholiths in Finland typically cover hundreds to thousands of km^2 in surface area and can reach thicknesses of more than 10 km (Elo and Korja 1993). The Vehmaa Batholith is composed of multiple rapakivi intrusions emplaced between 1.58 and 1.57 Ga (Lindberg and Bergman 1993), spanning an area of roughly 700 km^2 (Selonen et al. 2005). The outer, largest and oldest parts of the Vehmaa Batholith are dominated by pyterlite (a local name given for a variety of granitic rock that contains some ovoidal potassium feldspar megacrysts; see Rämö and Haapala 2005). The central part of the batholith contains three smaller rapakivi intrusions composed of medium-grained porphyritic intrusions, surrounded by a separate coarse-grained porphyritic intrusion. Fine- to medium-grained aplitic intrusions are widespread across the entire Vehmaa body but predominantly occur along the contacts of the multiple intrusions within the batholith and along its margins. The mineralogy across the batholith is relatively uniform, consisting of potassium feldspar, quartz, plagioclase, and biotite. Hornblende is only present in pyterlite (Selonen et al. 2005).

Geochemical composition of the porphyritic rapakivi indicates fractional magmatic crystallization (Karell et al. 2009), while evidence of late magmatic and hydrothermal processes can be found in the form of miarolitic cavities, quartz veins, and greisens (Selonen et al. 2005). Anisotropy of magnetic susceptibility (AMS) data indicate: (i) gentle dip of the tabular intrusive bodies away from the center of the batholith; (ii) moderate outward dip of contacts with the host rock; and (iii) youngest magmatic pulses within the batholith center. These findings could support either piston-like cauldron subsidence (Selonen et al. 2005; Karell et al. 2009) or sheet-like pulsing, as seen in the concentric Götemar pluton in Sweden (Mattsson et al. 2024). Due to the anorogenic character of the Vehmaa Batholith, no syn-magmatic tectonic fabric is evident. Therefore, these AMS anisotropies result from the emplacement of the igneous body. Additionally, thermobarometer data indicate that the emplacement of the Salmi, Wiborg and Åland batholiths occurred at upper crustal levels, of 4 to 12 km, suggesting a similar depth range for the emplacement of Vehmaa (Fig. 1; Eklund and Shebanov 1999). Breccias and substantial fracturing are not commonly reported at the contact margins of rapakivi bodies in Finland. Instead, these contacts are typically sharp or gently undulating (Rämö and Haapala 1995; Haapala 1997; Karell et al. 2009), suggesting that the surrounding host rocks accommodated the emplacement of the rapakivi bodies without significant brittle deformation.

Methods and data

We employ a multiscale analysis approach to assess the formation of crystalline geothermal reservoirs within the Vehmaa Batholith. At a regional scale, we use airborne LiDAR, bathymetric maps, and aerogeophysical data to delineate km-scale structures that transect the Batholith and surrounding regions (Fig. 2a–c). At the meso-scale, we combine the remote sensing data with structural information obtained from UAV-based photogrammetry to map structures from hundreds of meters down to structures of tens of centimeters. At the outcrop scale, our focus was on identifying and mapping brittle structures and associated mineral alteration intervals (Fig. 3). Additionally, we performed paleostress analysis to evaluate the fault kinematics, as mapped at the outcrop scale, within the Vehmaa Batholith. This analysis was cross-referenced with information from the brittle deformation stages and structural orientations documented in the Åland Rapakivi Batholith (Nordbäck et al. 2024).

Remote sensing mapping

Lineament mapping

Lineament mapping was conducted at two scales (i) 1:500 000, with the aim of understanding the contrasts and similarities between structures within and around the Vehmaa Batholith, and (ii) 1:200,000 scale, focusing on a more detailed interpretation of structures that transect the rapakivi intrusion. Interpretations at both scales were based on a 2 m/pixel resolution airborne LiDAR data produced by the National Land Survey of Finland (2019), combined with bathymetric data (Fig. 2a) collected at a 115 m/pixel resolution (EMODnet Bathymetry Consortium 2018). Additionally, we used airborne

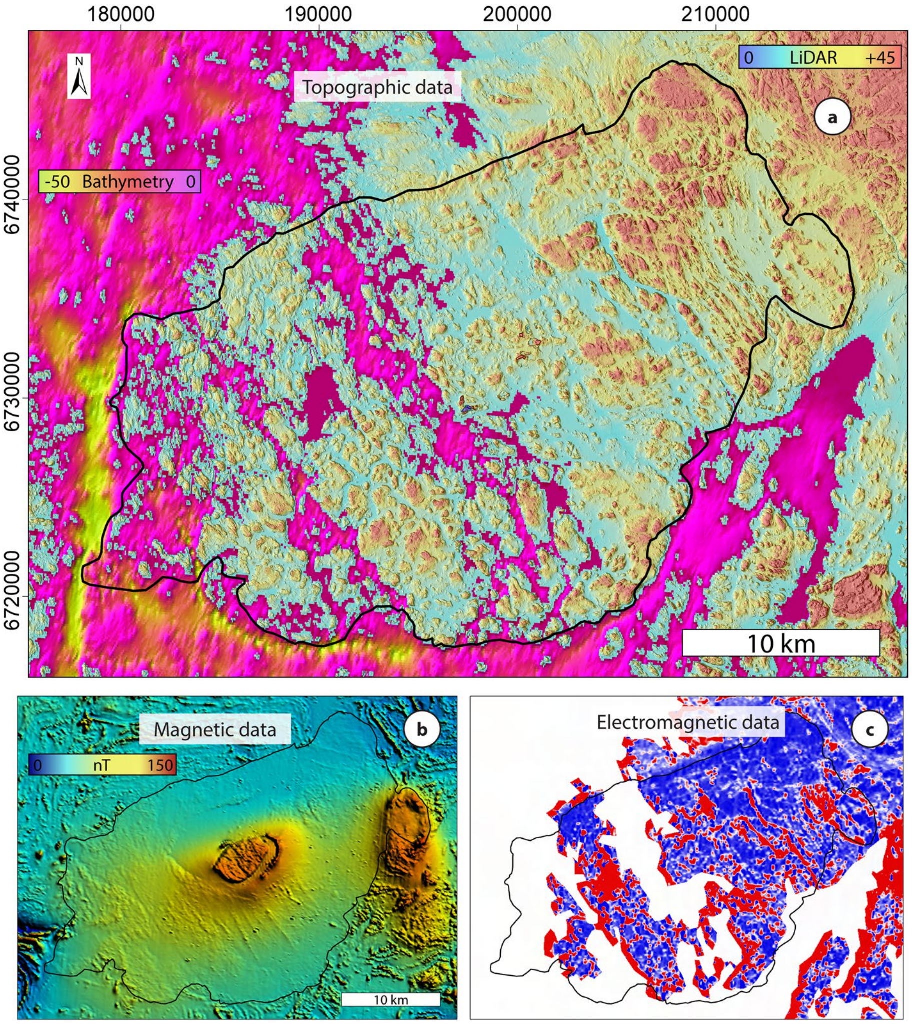

Fig. 2 Remote sensing source datasets. **a** Topographic LiDAR (*blue–red* color scale) and bathymetry data (*magenta–blue* color scale). **b** Magnetic data (*red–blue* color scale). **c** Electromagnetic data (imaginary component; *blue–red* color scale). *Black polygon* = outline of the Vehmaa Batholith

magnetic (Fig. 2b) and electromagnetic datasets (Fig. 2c) with a pixel resolution of 200 m collected by the Geological Survey of Finland (GTK) (Hautaniemi et al. 2005; GTK 2007a, 2007b). Initially, each dataset was interpreted separately, and then combined into a single integrated lineament map following the workflow described in Nordbäck et al. (2023) and Engström et al. (2025). This detailed integrated map was then compared with field structural observations from over 40 locations across the Vehmaa Batholith, aiming to validate the geological significance of the lineaments (Fig. 4).

UAV mapping

Based on the locations, extension, and connectivity of lineaments (see Sect. 3.3), as well as the availability of substantial outcrop exposures, UAV surveys were conducted at seven locations, with four key sites selected for detailed UAV fracture mapping. These locations cover both the central part and the contact margin of the Vehmaa Batholith.

Fig. 3 Field mapping of fault zones in the Vehmaa Batholith. **a** Strike-slip fault associated with mineral alteration marked by the *reddish coloration*. **b** Example of a joint network with multiple orientations. **c** A SE-striking fault plane associated with a weak sub-horizontal fault lineation and observable secondary porosity. **d** A S-striking fault plane with well-marked oblique slickenlines. The fault surface also exhibits steps, which are useful for determining the sense of slip (slickenline orientation and the dextral sense of movement on the fault surface are visualized with the *yellow arrow*). In both images **c** and **d**, the compass lid and body edge trends to the south

At three sites, areas of ~360 to 600 m^2 were surveyed from an altitude of 10 m, achieving an average ground sampling distance (GSD) of 0.275 cm/pixel (for detailed methodology see Ovaskainen et al. 2022). A larger site of approximately 19,200 m^2 was imaged from an altitude of 20 m. Additionally, we documented two smaller sections of an outcrop from a 3-m altitude, capturing the relationship between mineral alteration and fracturing. The images were processed in Agisoft Metashape and georeferenced using 6–10 VRS-GPS ground control points collected at each surveyed outcrop.

After processing the orthomosaics, we used the ArcGIS software to digitize linear traces corresponding to fractures in the crystalline bedrock and polygons highlighting altered areas of the bedrock. This generated 2D fracture networks showing the

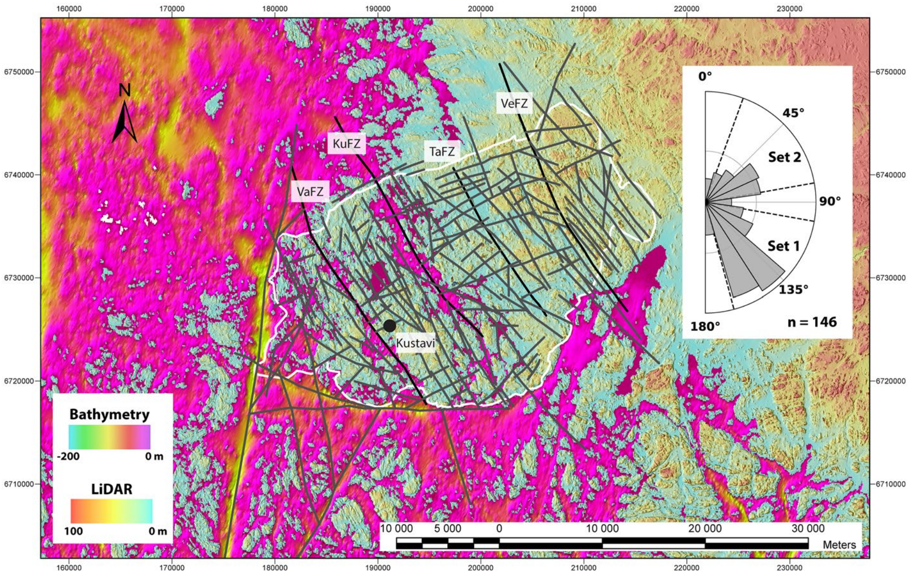

Fig. 4 Integrated lineaments interpreted from topographic and geophysical datasets at 1:200,000 scale within the Vehmaa Batholith (outlined in *white*). Lineaments are overlaid on a combined raster background of LiDAR (*blue–red* color scale) and bathymetry (*magenta–blue* color scale). Four major NNW-trending lineaments are highlighted in *black*: *VaFZ* Vartsala Fault Zone, *KuFZ* Kustavi Fault Zone, *TaFZ* Taivassalo Fault Zone and *VeFZ* Vehmaa Fault Zone. Other lineaments are shown in *dark grey*. The *rose diagram* illustrates the distribution of lineament trend orientations, grouped into dominant sets (Set 1 and Set 2) as indicated by *dashed boundaries*

location, extent, and connectivity of fractures at each studied location. Depending on outcrop quality, the 0.27 cm/pixel resolution typically allowed capturing individual fractures as small as 10 cm in length while the limited lateral extent of many outcrops led to censoring of trace lengths of longer fractures. To enable topological analysis of the fracture network, the digitization process adhered to the recommendations outlined by Nyberg et al. (2018).

Field mapping

We mapped fractures of different origins across the field area. Brittle discontinuities with no reference to their origin are here referred to as ‘fractures’. ‘Joints’ describe fractures that lack evidence of shear displacement between adjacent wall rock blocks. ‘Fault’ is used exclusively for structures associated with shear displacement. Faults displaying a damage zone adjacent to one or multiple fault cores are here termed fault zones, following the schemes proposed in Mitchell and Faulkner (2009) and Peacock et al. (2016), while ‘fault system’ is reserved for a network or group of related faults that occur in a specific geological region and often share a common origin, stress regime, or structural history. In this study, the terms fault zone and fault system are used in a scale-independent manner, and we recognize them both at outcrop and regional scales.

Structural mapping focused on roadcuts and coastal outcrops, where fracture planes could be observed at scales of up to tens of meters, and in many cases, in three dimensions (Fig. 3). Faults, joints and fractures were mapped at nearly 40 key locations across the Vehmaa Batholith. For all mapped fractures, we recorded their plane orientation (DipDir-Dip), density, presence and type of mineral infill, evidence of alteration, relationships among structural elements, and visible porosity at outcrop scale (Fig. 3c). To account for the magnetic declination, 9° were added to all compass measurements. For faults, a complete kinematic dataset was collected, including the orientation of fault planes and slip lineation, sense of kinematic movement (Fig. 3d), and the degree of certainty of these kinematic observations (high, moderate, or low; Table 2). The fault kinematic dataset is presented in Appendix A.

Lineament and fracture network analysis

To conduct a comprehensive multi-scale analysis of lineament and fracture network characteristics, we utilized fractopo, an open-source tool for geometric and topological fracture network validation and characterization, following its application in comparable geological settings (Ovaskainen et al. 2022; Nordbäck et al. 2023; Ovaskainen 2023). Fractopo operates within a user-defined target area, where all lineament and fracture traces are clipped for analysis. As a result, all statistics and visualizations presented here are derived exclusively from structures contained within these target-area boundaries. Fracture and lineament orientations are displayed using equal-area, length-weighted rose diagrams, in line with the recommendations of Sanderson and Peacock (2020). These diagrams facilitate the classification of traces into dominant orientation sets with boundaries defined according to the prevailing trends observed in both lineament interpretations and outcrop measurements to capture orientation clustering.

Fracture network density was assessed using P_{21} fracture intensity which corresponds to the total length of fractures per unit area. Connectivity was analyzed by calculating connections per branch (C_B). These parameters were visualized through 1-m-resolution contour grids following the approach of Nyberg et al. (2018). Higher P_{21} values generally reflect zones of increased permeability, while C_B provides a first-order measure of fracture network connectivity. To compare connectivity across scales and data types, node type proportions (X, Y, I) are presented in ternary plots, as outlined by Manzocchi, (2002). Additionally, dimensionless branch intensity (B_{22}) values were calculated for each target area, offering a scale-independent metric of fracture intensity (Sanderson and Nixon 2015).

Paleostress analysis

Using paleostress analysis we aim to unravel the past stress conditions that produced the brittle deformation of the rock, and to interpret the relationships between stress fields and the development of high-permeability structures. In mechanically isotropic materials, fault slip is typically aligned with the direction of the maximum shear stress, a concept known as the Wallace–Bott hypothesis (Wallace 1951; Bott 1959). Under such conditions, fault-slip data provide valuable insights for conducting paleostress inversion analyses (Angelier 1994; Lacombe 2012; Pascal 2021). Overall, the Vehmaa Batholith comprises homogeneous and non-foliated rocks with minor texture variation; thus, exhibiting dominant isotropic properties at a mesoscopic scale of meters to hundreds of meters. This minor compositional and textural heterogeneity makes it an ideal location for applying Wallace–Bott principles to determine the paleostress orientation at the time of the formation of the brittle structures. Furthermore, the anorogenic character and age of emplacement, postdating major orogenic events such as the Svecofennian orogeny (1.9 to 1.8 Ga), contribute to the absence of significant mechanical anisotropies in the Vehmaa Batholith.

Stress tensor calculations, including the orientation and relative magnitudes of principal stresses, were performed using the 'WinTensor' software (Delvaux and Sperner 2003). The WinTensor software evaluates the quality of the resolved stress tensors, assigning ratings from A to E. This evaluation considers various factors, including the quantity of data, the deviation in slip, the confidence in slip sense for individual faults, and the type of data used (Delvaux and Sperner 2003). Relative magnitudes were calculated as the stress ratio R ($\sigma_2 - \sigma_3/\sigma_1 - \sigma_3$), which describes the character of the stress regime and the type of faulting (Delvaux et al. 1997). To divide our structural dataset into subsets and calculate the paleostresses evolution of the study area, we apply the workflow detailed in Nordbäck et al. (2024) and Mattila and Viola (2014). Thus, the preliminary categorization of our fault-slip data into subsets using the right dihedron method was followed by the iterative "rotational optimization" method to determine the optimal stress tensor for each sub-set. During the rotational optimization phase, any data with a misfit angle greater than 30° between the observed and theoretical slip directions (as predicted by the stress tensor) was considered incompatible and discarded from our subsets. The incompatible data points were then either reassigned to a different sub-set or excluded from further analysis.

Sixty-nine fault kinematic observations were collected in the field. Of these, the sense of slip was determined for 68 faults. The reliability of these kinematic observations was classified as high (N = 25), moderate (N = 30) and low (N = 13). In addition, nine of these measurements were discarded during WinTensor validation due to an angular field measurement error greater than 20° between the lineation and fault plane. Thus, we used a total number of 58 observations for paleostress analysis.

Results

Lineament analysis

Our integrated 1:200,000-scale lineament interpretation (Fig. 4) highlights two dominant orientations: Set 1 includes NW–NNW structures trending 100°–165° and Set 2 encompasses ENE structures trending 20°–80°. Structures in Set 1 generally show greater continuity with typical lengths around 10 km and some reaching up to 27 km. In contrast, Set 2 consists of shorter, more discontinuous features, with only two lineaments longer than 10 km.

Within Set 1, four major NW-trending fault zones were recognized in the Vehmaa Batholith: the Vartsala (VaFZ), Kustavi (KuFZ), Taivassalo (TaFZ), and Vehmaa Fault Zones (VeFZ). These zones exhibit slight curvature and occur at a consistent spacing of approximately 7 km. Except for TaFZ, all are over 25 km in length and extend from the rapakivi granite into the surrounding host rock. VaFZ and KuFZ are located in the offshore western part of the batholith and are therefore only partially exposed on a series of islands. In contrast, TaFZ and VeFZ are situated onshore in the eastern part of the batholith (Fig. 4).

In addition to these major structures, minor NW-trending lineaments are present throughout the batholith. Some of these appear as secondary features that connect or branch off from the major NW-trending structures, such as at step-overs and horsetail terminations. The area southwest of the VaFZ shows a rather different structural pattern, with predominant WNW (Set 1) and NE (Set 2) lineaments. In the southeastern part of the batholith, where outcrop exposure is more extensive, a cluster of shorter Set 1 lineaments appears proximal to the VeFZ. This southeastern area lacks Set 2 lineaments (Fig. 4).

Set 2 lineaments are particularly common in between VeFZ and KuFZ within the northern part of the batholith, whereas their spatial occurrence is more scattered in other parts of the batholith. Set 2 structures commonly terminate against Set 1 structures, suggesting that they are younger (see e.g., Peacock et al. 2017; Li et al. 2024). An exception to the topological relationship occurs in the TaFZ, which is intersected by multiple Set 2 lineaments up to 10 km long (Fig. 4).

Regionally, the orientation of the NNW and ENE-trending lineaments within the Vehmaa Batholith differs from the NNE and ENE lineaments within the surrounding Paleoproterozoic bedrock (Fig. 1). An exception occurs northeast of the Vehmaa Batholith, particularly near the Laitila Batholith and the Kynsikangas Shear Zone, where lineament orientations are largely similar to those within the Vehmaa Batholith, at least partly due to the prominence of KySZ that has an NNW–SSE orientation (Fig. 1).

Despite the discontinuous nature of many Set 2 lineaments, collectively both lineament sets form a connected network across the Vehmaa Batholith. The mapped lineament network produces a connections per branch (C_B) value of 1.69 (Fig. 11), indicating a moderately interconnected fault network where each fault branch, connects to an average of 1.69 other branches. The overall lineament intensity (P_{21}) at 1:200,000 scale, quantifying the total length of lineaments per unit area, is only 0.001. However, the dimensionless intensity (B_{22}) of 1.96 suggests that, relative to the area, the network has a high intensity.

Field and UAV observations

In total, we measured and analyzed the orientations and kinematic indicators of 69 faults and 509 joints. Figure 5 presents the orientation data compiled from mapped lineaments, outcrop faults, and joints. The NNW-trending Set 1 is prominent among the lineaments and faults, but is less distinct within the joint population. In contrast, the NE-trending Set 2 is more consistently observed across joint networks and outcrop faults. Additionally, in some outcrops, we identified an E-trending fault set, referred to as Set 3. Most of the mapped faults and joints are subvertical or steeply dipping. Fracture network intensity and connectivity data are summarized in Table 1.

Site 1: Central Vehmaa Batholith

Site 1 (Fig. 5) was surveyed using UAV photogrammetry at a flight altitude of 20 m, covering a large, partially exposed outcrop approximately 130 × 170 m in size. Due to incomplete outcrop exposure, fracture mapping was limited to fractures longer than 10 m (Fig. 6a, b). The longest fractures at Site 1 exhibit orientations broadly consistent with the dominant local lineament trends, particularly a NW-trending Set 1 and a NE-trending Set 2 (Fig. 6a, c), with a subordinate E-trending Set 3 also present (Fig. 6a).

Field mapping revealed hydrothermal alteration along several Set 1 and Set 3 fractures, including pervasive precipitation of epidote and chlorite. Three major structures were

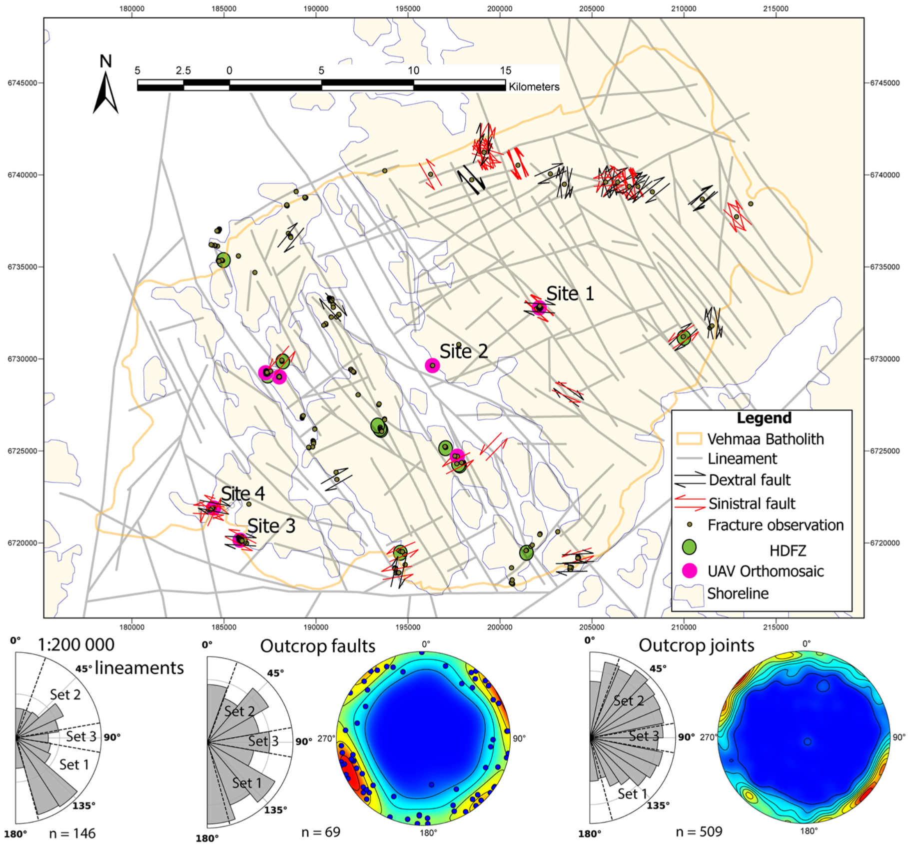

Fig. 5 Structural framework of the Vehmaa Batholith showing mapped lineaments, fault-slip observations, fracture observations, and UAV orthomosaic sites. Lineaments are interpreted from airborne LiDAR and geophysical data. Field observations include dextral (*black*) and sinistral (*red*) faults based on kinematic indicators. The *orange polygon* outlines the Vehmaa Batholith. *White area* represents offshore. For comparison, the orientation of lineaments, outcrop faults and outcrop joints are displayed as *rose diagrams*. Due to the lack of information on lengths, the fault and joint data were not length normalized. *Green dots* mark the location of identified high-density fracture zones (HDFZ)

interpreted as faults based on offset indicators and alteration halos: two sinistral faults within Set 1 (up to 90 m in length) and one dextral fault associated with Set 3.

The fracture network at Site 1 includes both large-scale individual fractures and clusters of closely spaced joints. Several of the mapped fractures reach lengths of at least 90 m that transect all the area of the survey, indicating substantial lateral continuity. In many areas, fractures occur in sets where individual fractures are spaced only centimeters to tens of centimeters apart (Fig. 6b). Although Site 1 provides important qualitative insights into fracture orientation and hydrothermal features, the incomplete exposure of the outcrop limits the quantification of network connectivity and intensity. Thus, fracture network parameters from this site are not included in Table 1.

Site 2: contact zone of pyterlite and porphyritic granite

Site 2 is located near the contact between coarse-grained pyterlite and medium-grained porphyritic granite (Fig. 5). The shoreline outcrop comprises a complex assemblage of lithologies, including pyterlite, fine-grained aplitic dykes, and quartz veins hosting

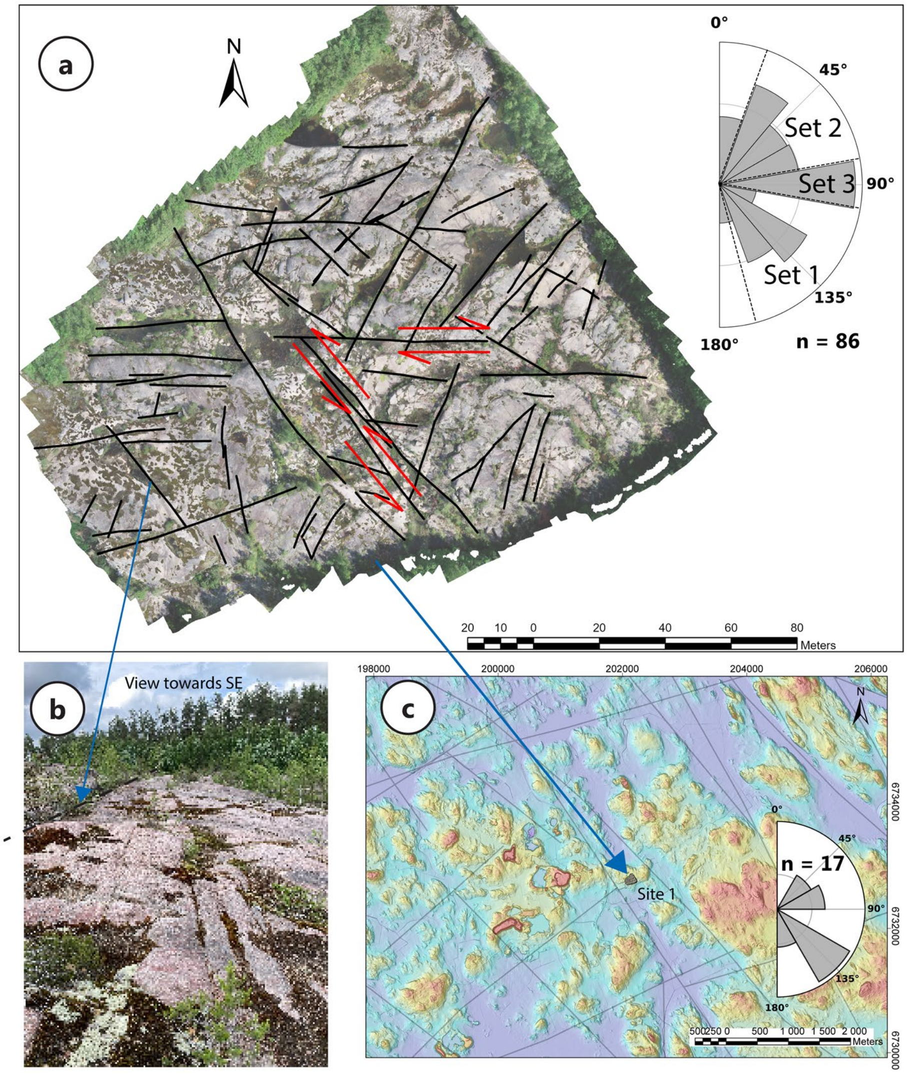

Fig. 6 Multiscale structural analysis of Site 1, linking outcrop observations with UAV and regional data. **a** UAV orthomosaic of Site 1 (surveyed from 20 m altitude), showing digitized fracture traces (*black*), and fault kinematics indicated by *double-headed arrows*. A *rose diagram* summarizes fracture orientations, grouped into three dominant sets. **b** Field photograph from the southwestern edge of Site 1, looking southeast. The location of the *dotted fracture trace* is indicated by an *arrow*. **c** Digital elevation model from airborne LiDAR data, showing the structural framework around Site 1. *Grey lines* represent interpreted lineaments. The *rose plot* shows the orientation of lineaments within a 4 km radius from the site

miarolitic cavities—features commonly associated with late-stage magmatic and hydrothermal processes (Fig. 7a, b). Fracture orientations at Site 2 are broadly consistent with those at Site 1 (Fig. 6a) and align well with the dominant local lineament trends. However, due to the greater length of NNW-trending lineaments, these appear dominant in the length-weighted rose plot (Fig. 7c). The shape and orientation of the shoreline itself appear structurally controlled, reflecting the influence of persistent fracture sets on landscape morphology.

No major faults were identified at Site 2 or in the surrounding area. However, the outcrop displays a dense network of small-scale fractures, with individual lengths reaching up to 10 m. The continuity of many fracture traces beyond the narrow

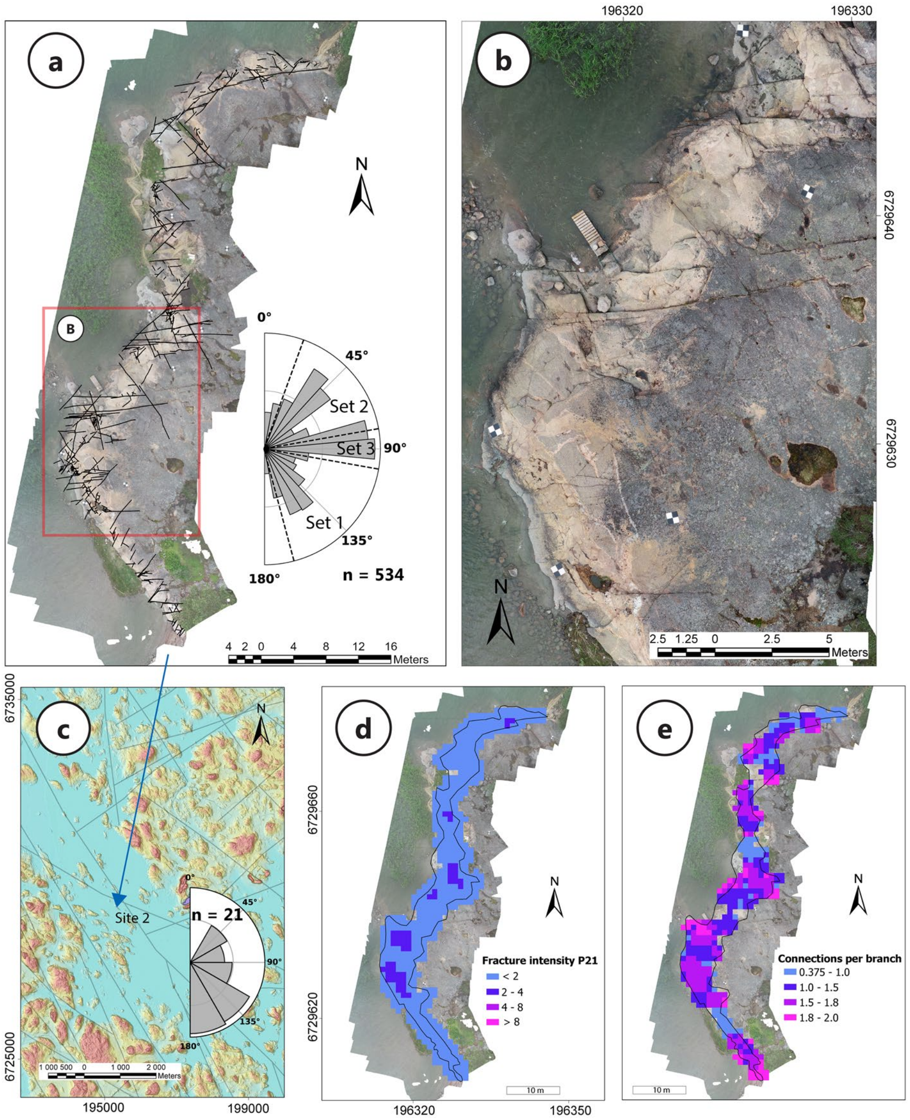

Fig. 7 Structural analysis of Site 2 from UAV. **a** Orthomosaic showing digitized fractures traces, with their orientations summarized in the *rose diagram*. **b** Zoomed-in view of a section of Site 2 orthomosaic; location shown in *red* in **a**. **c** LiDAR DEM and interpreted lineaments (*grey lines*) in the surrounding regions of Site 2. The *rose plot* shows the orientation of lineaments within a 4 km radius from the site. **d** Fracture intensity contour map (P_{21}) calculated using a 1 m grid. **e** Fracture network connectivity map showing the connections per branch (C_B), calculated using a grid size of 1 m

outcrop width (~5 m) suggests longer structures that extend outside the surveyed area (Fig. 7b). Fractures frequently occur in subparallel sets with close spacing—ranging from a few centimeters to several tens of centimeters, particularly within the aplitic portions of the exposure.

Quantitative analysis of the fracture network indicates an average fracture intensity (P_{21}) of 1.44 m/m^2, with localized values reaching up to 3.88 m/m^2 (Fig. 7c). Fracture connectivity, as expressed by the average connectivity parameter (C_B), is 1.49 (Fig. 11), while the dimensionless fracture intensity (B_{22}) is 0.69 (Table 1).

Site 3: southwestern contact of the Vehmaa Batholith

Site 3 is located within pyterlite at the southwestern contact of the Vehmaa Batholith (Fig. 8). The fracture network is characterized by a well-defined orthogonal pattern formed by Set 1 and Set 2 joints. Set 1 fractures are longer and more continuous—reaching lengths of up to 17 m—while Set 2 fractures frequently terminate against Set 1, suggesting a hierarchical fracture arrangement. The local lineament pattern surrounding Site 3 closely mirrors these outcrop-scale fracture orientations (Fig. 8c), indicating structural coherence across scales. No clear faulting or hydrothermal alteration was observed within the UAV-surveyed area. However, a partially exposed SE-striking sinistral fault was identified just northeast of the site and can be traced for approximately 300 m in LiDAR data. Additionally, a smaller E-striking dextral fault is located to the east of the outcrop (Fig. 8c), suggesting the area is structurally influenced even if faults are not directly exposed or easily identified in the survey area.

Fracture intensity (P_{21}) ranges from 0 to 4.87 m/m^2, with an average of 1.72 m/m^2 (Fig. 8d; Table 1). Due to the abundance of Set 2 fractures that interconnect the longer Set 1 structures, the overall connectivity of the fracture network is relatively high. Most parts of the outcrop exhibit C_B values above 1.5, with an average C_B of 1.78. The dimensionless fracture intensity (B_{22}) is 1.17 (Figs. 8e, 11; Table 1).

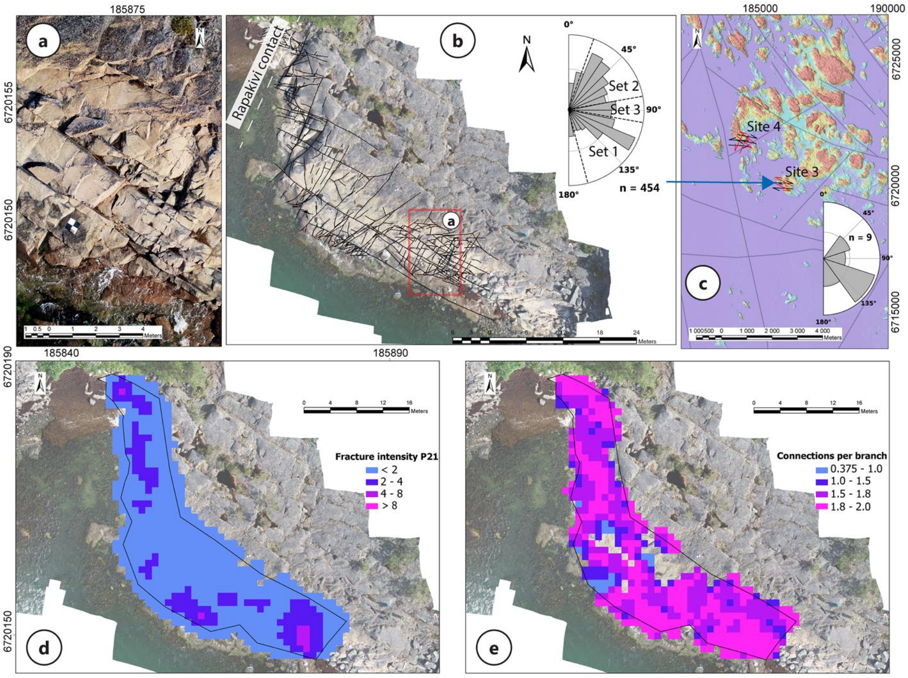

Fig. 8 Structural analysis of Site 3 based on UAV and outcrop data. **a** Zoomed-in view of a section of the outcrop shown in *red* in **b**. **b** UAV orthomosaic of Site 3 showing digitized fracture traces, with their orientations summarized in the *rose diagram*. The position of the rapakivi contact is marked with a *dotted white line*. **c** Interpreted lineaments (*grey lines*) and mapped faults (*double arrows*) overlaid on the LiDAR DEM in the surrounding regions of Site 3. The *rose plot* shows the orientation of lineaments within a 4 km radius from the site. **d** Fracture intensity contour map (P_{21}) calculated using a 1 m grid. **e** Fracture network connectivity map, showing connections per branch (C_B) based on a 1 m grid

Site 4: southwestern contact of the Vehmaa Batholith

Site 4, located approximately 5 km northwest of Site 3 and near the southwestern margin of the Vehmaa Batholith (Fig. 5), shows a strong spatial association between fracturing, hydrothermal alteration, and generation of secondary porosity. As observed at Site 3, the dominant fracture sets are NE-trending (Set 2) and ESE-trending (Set 1; Fig. 9a). While these orientations differ slightly from the broader lineament trends observed within the batholith (Fig. 5), they are consistent with more localized lineaments in the southwestern area (Fig. 8c). The longest mapped Set 1 fractures reach up to 11 m in length, although limited outcrop exposure prevents tracing their full extent, as LiDAR data reveal that these structures can be traced for several kilometers. In contrast to the relatively uniform fracture network properties observed at Sites 2 and 3, Site 4 displays structurally controlled hydrothermal anomalies. Intensively fractured zones associated with Set 1 (WNW-striking) correspond to porous, hydrothermally altered bedrock at the surface exposures. These zones are frequently accompanied by thin, WNW-oriented mafic veins composed of chlorite and amphibole (Fig. 9b). These altered zones also show elevated fracture intensity and connectivity, with P_{21} values ranging from 0 to 10.42 m/m^2 (average 2.99 m/m^2), C_B averaging 1.72, and a B_{22} value of 0.76 (Table 1; Figs. 9c, d, Fig. 11).

Drone and field observations suggest that Set 2 fractures are less continuous and exert weaker control on alteration, although they are present within altered domains and often intersect Set 1 fractures (Fig. 10). These intersections locally enhance network connectivity and contribute to the high fracture intensity in structurally complex areas. Several of the altered Set 1 zones were identified as faults, though their kinematic characteristics vary. One fault zone (Fig. 10a, c) exhibits sinistral shear with a well-defined fault core and surrounding damage zone that includes antithetic and extensional fractures. Another fault (Fig. 10b, d) displays approximately 30 cm of dextral displacement along an aplite vein. Many of the Set 1 fault planes also show evidence of mineral precipitation and mafic veins, indicating sustained fluid flow along these structures. In contrast, such mineralization and veining are absent in the extensional components of these structures, suggesting that fault formation predated the hydrothermal event (Fig. 10a, c). Beyond these two fault zones, we interpret a 5-m-wide, intensely fractured and altered corridor in the central part of Site 4 (Fig. 9a) as a fault zone. Due to its highly heterogeneous and disrupted character, a clear kinematic interpretation could not be established.

High-density fracture zones

High-density fracture zones (HDFZs) were observed at eight distinct locations across the Vehmaa Batholith (Fig. 5). These zones consist of sets of closely spaced (mm- to cm-scale), open fractures that often form linear or anastomosing patterns at the outcrop scale (Fig. 12). The orientation and spatial distribution of these zones are commonly aligned with strike-slip faults, indicating strong structural control on their formation. Without exception, HDFZs strike roughly orthogonal to major NNW-trending lineaments, suggesting they may represent subsidiary structures that branch off from principal fault zones (Fig. 5). Their orientations are consistent across all mapped locations, supporting a regionally persistent structural control. Due

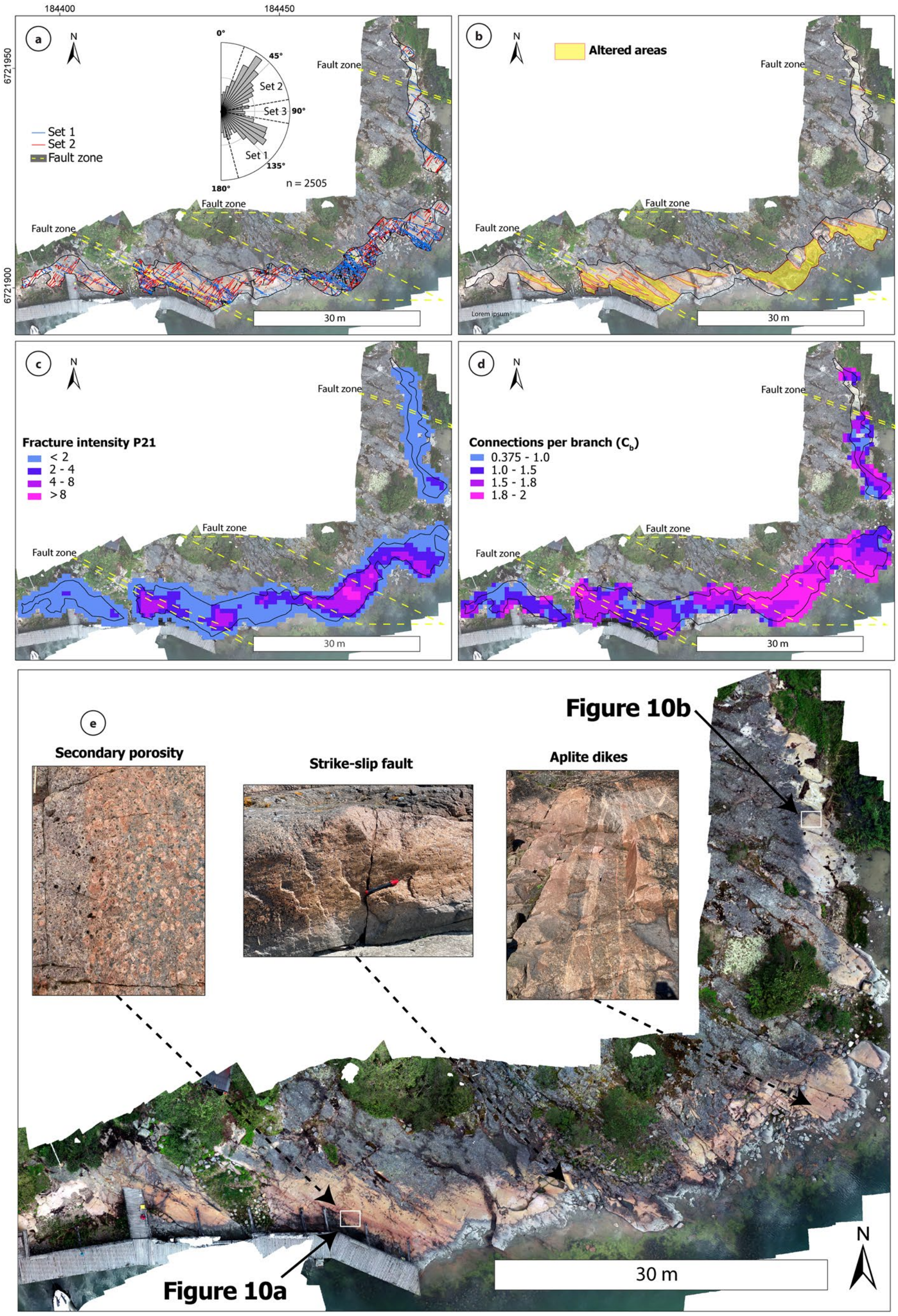

Fig. 9 UAV-based fracture trace analysis from Site 4 outcrops. **a** Digitized fracture network, with northeast-trending fractures (Set 1: 30°–60°) shown in *red* and east-southeast-trending fractures (Set 2: 105°–145°) in *blue*. Interpreted fault zones are *outlined with dashed lines*. A rose diagram summarizes fracture orientations for the site (n = 2505). **b** Digitized polygons showing visually identified zones of altered bedrock (*yellow*). **c** Fracture intensity (P_{21}) contour map calculated using a 1 m grid. **d** Fracture network connectivity (connection per branch, C_B) calculated using a 1 m grid

to limitations in analyzing the cores of major ENE-trending lineaments, which are often unexposed or submerged beneath the Bothnian Sea, we are unable to determine

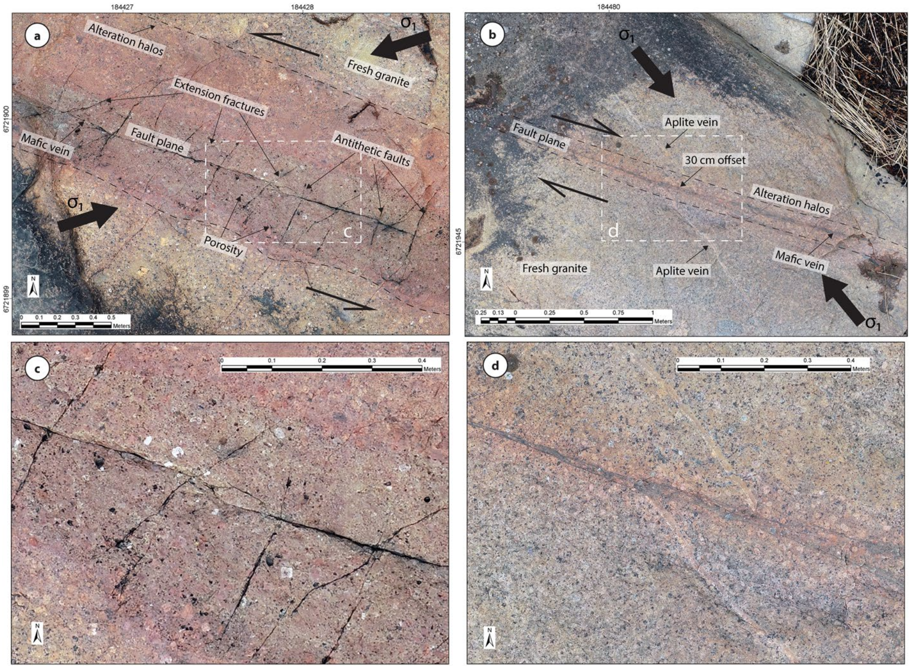

Fig. 10 Field examples from Site 4 showing the spatial relationship between faulting and hydrothermal alteration. Southeast-striking strike-slip faults display alteration halos up to meter-thick, symmetrically developed on both sides of the fault plane and oriented parallel to it. **a** Sinistral strike-slip fault with a prominent alteration zone (*reddish coloration*), spatially associated with the intersection of the SE-striking main displacement zone and a damage zone consisting of secondary fractures—interpreted as possible extension fractures and antithetic faults—that crosscut it at a high angle. Secondary porosity is visible as *black dots* at the outcrop surface. **b** Fault plane with a chlorite and amphibole vein and surrounded by a 30-cm-wide alteration halo. An aplite vein if offset by approximately 30 cm in apparent dextral sense. Panels **c** and **d** show zoom-ins to **a** and **b**

whether these HDFZs are exclusive to NNW-striking structures or if they also occur along ENE-striking faults.

Combining field observations with high-resolution LiDAR data, we found that HDFZs are arranged in regular, subparallel sets, spaced from a few meters to several tens of meters apart. Individual fracture clusters typically range from tens of centimeters to a few meters in width, and in many cases, can be traced continuously over a kilometer along strike, indicating notable lateral continuity and strong structural coherence within the batholith (Fig. 12). The presence of HDFZs transecting the Vehmaa Batholith may significantly enhance rock permeability, acting as pathways that facilitate subsurface fluid flow and promote mineral alteration, as reported in various rock types worldwide (Questiaux et al. 2010; Sanderson and Peacock 2019; de Joussineau 2023; Bischoff et al. 2024).

Sub-horizontal sets of HDFZs were also identified at two locations, where no clear relationship with the main fault zones transecting the Vehmaa Batholith could be established. These flat sheet-like structures could tentatively be interpreted as having formed by the unloading of the granitic body during exhumation. While a detailed analysis of their origin is beyond the scope of this study, their geometry and

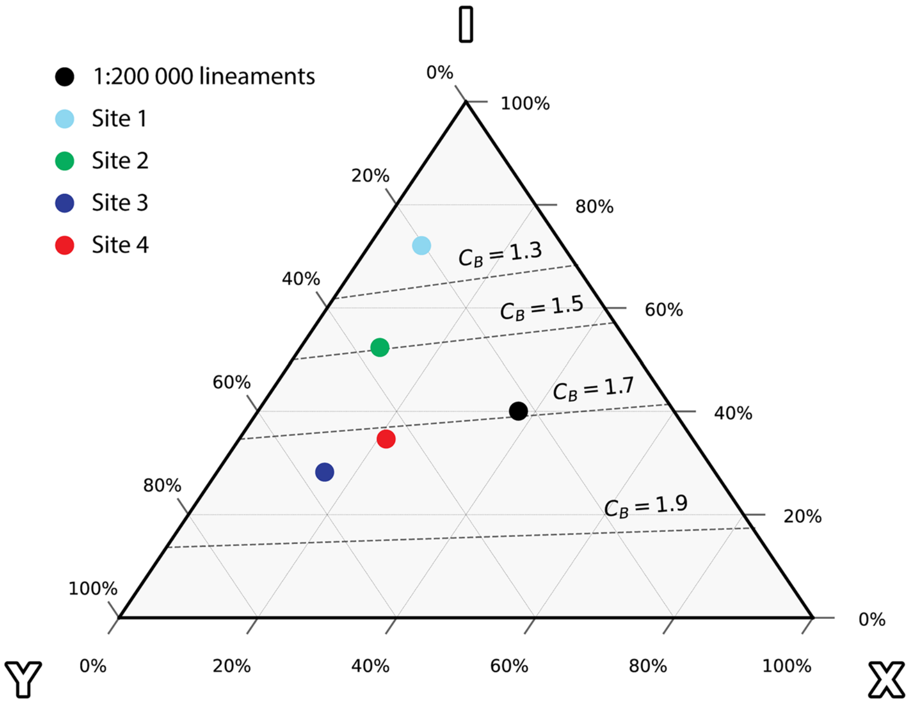

Fig. 11 Topological analysis of fracture networks based on UAV and lineament datasets, visualized as the relative proportion of node types: I-nodes (isolated ends), Y-nodes (branching points), and X-nodes (cross-cutting intersections). Each colored dot represents a dataset from Sites 1 to Site 4, and regional lineaments. *Gray dotted lines* represent values for connections per branch (C_B). Networks with more Y- and X-nodes show higher C_B values and better connectivity, which enhances fluid flow potential in crystalline geothermal reservoirs

orientation are consistent with flat lying joints typically associated with stress release in exposed crystalline rocks (Martel 2017; Penhoët et al. 2025).

Paleostress analysis

All 69 mapped faults within the study area exhibit strike-slip kinematics, characterized by steeply dipping main displacement zones (Fig. 5). Slip sense was determined for 68 faults, revealing a nearly balanced distribution: 36 faults show sinistral (left-lateral) movement, while 32 display dextral (right-lateral) motion. The sinistral faults predominantly strike NNW, aligning closely with the Set 1 lineaments, whereas the dextral faults mainly strike NE, corresponding to lineament Set 2 (Fig. 13). Using the WinTensor software for stress inversion, we identified two distinct strike-slip stress regimes, designated as Stage 1 and Stage 2. Stress tensors calculated from the entire dataset showed minimal variation compared to those based solely on high-certainty observations, underscoring the robustness of the inversion results. Figure 14 compares the paleostress tensors derived from (i) all kinematic data, (ii) only high-certainty data, and (iii) all data excluding low-certainty observations. Detailed tensor parameters are summarized in Table 2.

Stage 1 is characterized by a strike-slip regime dominated by sinistral Set 1 faults and dextral Set 2 faults, with the principal compressive stress (σ_1) oriented WNW–ESE (Fig. 14). The stress ratio (R), representing the relative magnitude of intermediate to maximum principal stresses, varies only slightly between 0.42 and 0.55 across

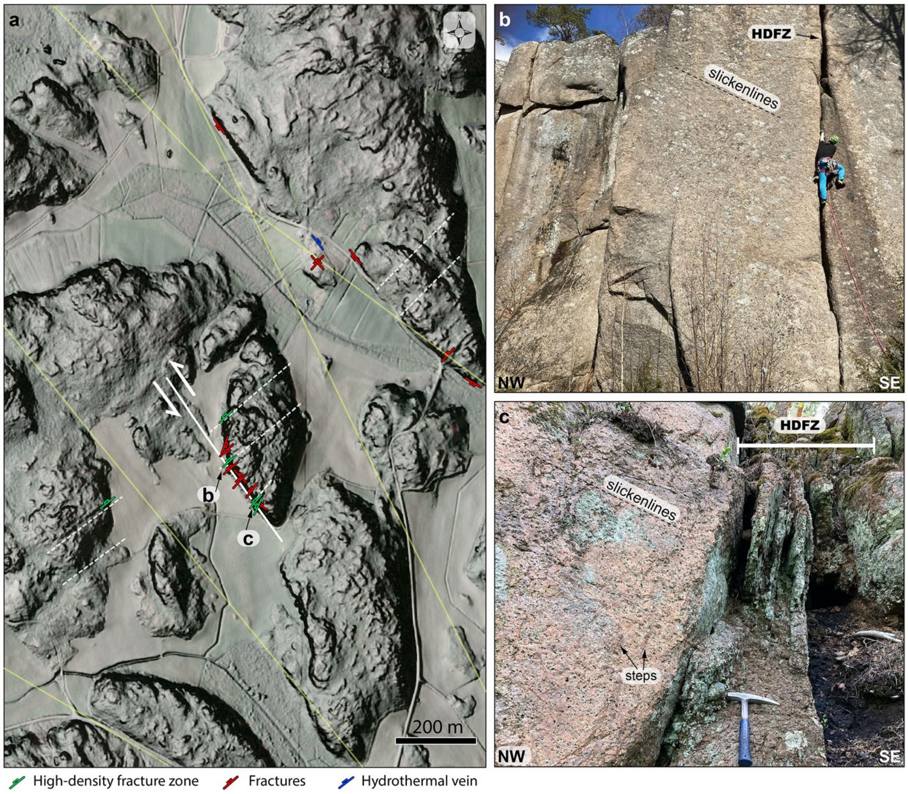

Fig. 12 Examples of high-density fracture zones (HDFZ) shown in LiDAR maps (**a**) and observed in the field (**b**, **c**), Central Vehmaa Batholith. *Yellow lines* represent lineaments from the integrated 1:200,000-scale map, while *white dashed lines* indicate the mapped extension of the HDFZ based on LiDAR data and field mapping. For the locations of these zones, refer to Fig. 5

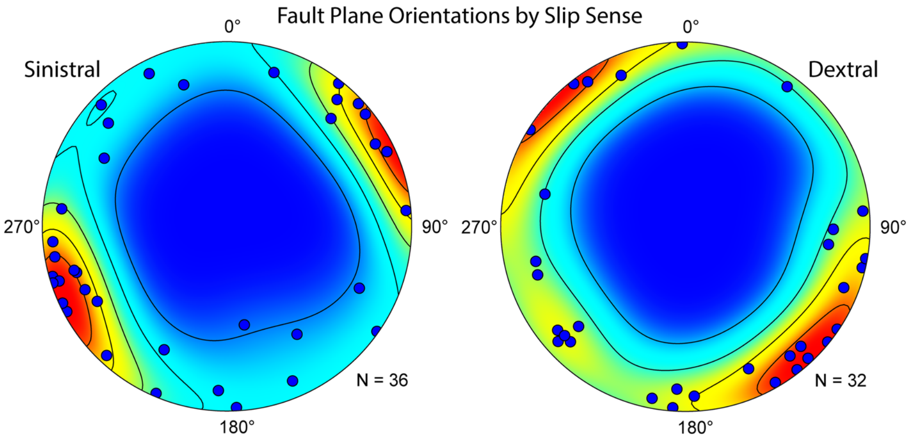

Fig. 13 Orientation data of the mapped fault planes, separated by kinematic sense of slip. The left stereonet shows sinistral faults (N = 36), while the right one shows dextral faults (N = 32). Contour plots represent the density of fault plane orientations

all datasets, indicating a stable and consistent pure strike-slip stress state for Stage 1. Notably, the tensor derived from the full dataset achieved the highest quality rating (A), reflecting strong confidence in this paleostress regime. At the time these structures

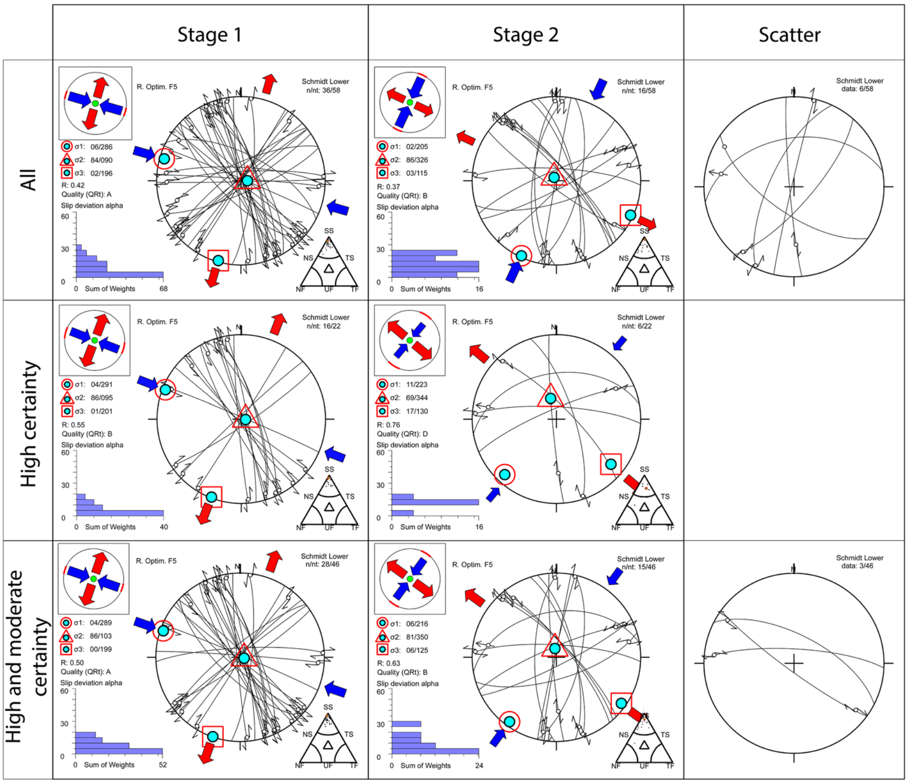

Fig. 14 WinTensor paleostress inversion analysis results for the Vehmaa Batholith, shown separately for all observations, high-certainty observations, and high- to moderate-certainty observations

formed, a stable stress field may have facilitated the development of steeply dipping fractures intersecting at various angles along these faults, creating a complex, interconnected network that represents promising targets for deep geothermal exploration (Sibson 1996).

Stage 2 comprises SE- to S-striking dextral faults (Set 1) and ENE-striking sinistral faults (Set 2), reflecting a strike-slip stress regime with a principal compressive stress (σ_1) oriented NNE–SSW, in contrast to the WNW–ESE compression observed in Stage 1 (Fig. 14). The stress ratio (R) varies depending on the dataset: 0.37 for all data (indicating a pure strike-slip regime), 0.76 for high-certainty observations (suggesting transtensional conditions), and 0.63 for combined high- and moderate-certainty data (consistent with pure strike-slip). The Stage 2 stress tensor derived from the full dataset has a quality rating of B, indicating slightly lower confidence compared to Stage 1.

Discussion

Timing of fault activity

Our paleostress inversion results show structural patterns consistent with observations from the Åland Batholith, where Stage 1 faulting was inferred to have occurred between 1.55 and 1.4 Ga, and Stage 2 around 1.3 to 1.2 Ga (Nordbäck et al. 2024). As in Åland, Set 1 structures in Vehmaa trend NNW and are more continuous, whereas ENE Set 2 structures are shorter and often terminate against Set 1 faults, supporting the interpretation that Set 1 faults are older (e.g., Peacock et al. 2017). Paleostress analysis in Vehmaa (Fig. 14) further supports previous studies of the Åland and Wiborg rapakivi batholiths, indicating that orthogonal joints formed after faulting and developed primarily within anisotropic bedrock influenced by pre-existing brittle structures (Skyttä et al. 2021; Nordbäck et al. 2024).

Despite the broadly similar structural patterns in the brittle deformation of the Vehmaa and Åland batholiths, the principal compression directions show some variation. In Stage 1, the σ_1 axis in Vehmaa trends 06/286°, approximately 15° offset from Åland, while in Stage 2 the difference increases to 28°. These discrepancies may reflect local variations imposed by structural inheritance from pre-existing regional structures. In Åland, large-scale faults align with older Paleoproterozoic shear zones such as the NW-trending Sottunga–Jurmo Shear Zone, whereas in Vehmaa, the dominant NNW-trending lineaments fit the NNW-trending of the Kynsikangas Shear Zone (Fig. 1; Ovaskainen et al. 2023; Nordbäck et al. 2024). Although these structural correlations suggest that strike-slip faulting in the Åland and Vehmaa batholiths may have been coeval, further age determinations of faults in both areas are required to confirm this interpretation.

Reservoir size, geometry, and connectivity

Brittle structures in Vehmaa show a strong correlation in orientation and spatial relationships across scales, from regional lineaments to outcrop-scale fractures (Fig. 5). At the outcrop scale, fault zones traceable for tens to hundreds of meters align with 1:200,000-scale lineaments extending up to 25 km (Figs. 6, 7, 8 and 9). This multiscale consistency indicates that the lineaments likely represent large fault systems (Tchalenko 1970; Bonnet et al. 2001) and, together with our analysis of fault connectivity, suggests that these structures may define kilometer-scale fractured reservoirs. The predominantly subvertical orientation of faults and most joints (Fig. 5) implies that these systems could extend several kilometers into the crust, consistent with strike-slip fault geometries (Bhattacharya 2022). Such vertical structures can strongly influence deep fluid flow within the crystalline crust, as illustrated by the Pontgibaud fault zone in the French Massif Central, where modeling suggests that a permeability of 1.6×10^{-14} m^2 could reach ~150 °C temperatures at 2.5 km depth (Duwiquet et al. 2019). In Vehmaa, comparable permeabilities may also be achieved in fault-controlled reservoirs (see "Geothermal exploration targets" section for details); however, such high temperatures are unlikely given the lower geothermal gradient of ~15–20 °C/km (Kukkonen et al. 2023), which would yield only ~50–60 °C at 2.5 km depth.

In detail, the Central Vehmaa Batholith is transected by multiple SSE- and NNW-trending lineaments that likely represent fault zones extending 10–25 km and continuing beyond the contact with surrounding Svecofennian rocks (Figs. 1, 4, 5). Longer faults are typically associated with wider damage zones and greater fracture densities. Based on scaling relationships, faults of 10–25 km length could produce 10–1000 m wide zones of highly fractured rock (e.g., Scholz et al. 1993; Scholz 2007; Vermilye and Scholz 1998), defining the largest reservoir volumes in the study area. Our LiDAR data show that most kilometer-scale lineaments are surrounded by topographic discontinuities, suggesting damage zones 100–200 m wide near the longest faults (Fig. 4). Additionally, P21 exceeds 10/m^2 near faults at Site 4, compared with values below 2/m^2 in more pristine parts of the rapakivi body (Table 1). Fracture connectivity exerts an equally important control on reservoir permeability, with C_B values at Site 4 reaching ~1.7, comparable to the average for lineaments and well above the 1.3 threshold generally considered favorable for continuous fluid pathways (Evans et al. 1997; Sanderson and Nixon 2018). Additionally, Site 4 and nearby lineaments display a higher proportion of X-nodes than other sites (Fig. 11), indicating a greater potential for fault intersections, consistent with observations from other fractured networks studies (Peacock et al. 2017; Peacock and Sanderson 2018).

To support the development of discrete fracture network (DFN) models, site-specific studies should investigate not only fracture intensity and connectivity, but also the length distribution of brittle structures. However, due to the censored nature and irregular shape of outcrops in Vehmaa, length distribution analysis was beyond the scope of this study.

Beyond fault-controlled fracture networks, orthogonal joint patterns in some more pristine host rocks also form well-connected networks, with C_B values exceeding 1.5 (Figs. 5, 11). Overall, joint lengths, orientations, and frequency are typically more scattered, and the dominant NNW trend observed in faults and lineaments is less pronounced (Fig. 5). These differences likely reflect contrasting deformation mechanisms, where faults accommodate displacement along discrete shear planes, whereas joints generally form under tensile stress and develop in multiple orientations influenced by local stress perturbations (Pollard and Segall 1987). From a geothermal perspective, this distinction is crucial: fault zones serve as primary conduits for fluid flow, while well-connected joint networks can increase effective reservoir volume, enhance overall permeability and recharge capacity, and potentially mitigate thermal short-circuiting during geothermal production (Zhang and Dahi Taleghani 2023). For instance, although no faulting was observed at Site 3, the orthogonal joint pattern and high connectivity values (Figs. 8, 11) suggest favorable pathways for fluid circulation. Similarly, at Site 2, fracture intensity and connectivity are elevated within aplitic dykes (Fig. 7), which likely acted as fracture-prone zones within the granite host. No significant brecciation or fracturing was observed at the contacts between the batholith and the surrounding paragneiss and migmatites, further suggesting that post-emplacement brittle deformation is the dominant process controlling the formation of fractured reservoirs in the Vehmaa body. However, since jointing typically decreases with depth in the crust, drilling data are needed to understand the brittle properties at depths.

Faulting and hydrothermal alteration

Hydrothermal alteration in the Vehmaa Batholith is manifested by fractures infilled with chlorite, epidote, and amphibole, as well as by color changes in the rock matrix adjacent to faults (Figs. 9, 10, and 15). This spatial association indicates that post-magmatic faulting played a primary role in forming fluid pathways and localizing hydrothermal alteration within the batholith. At multiple locations, alteration has led to mineral dissolution and the development of secondary porosity (Fig. 10), processes that enhance fluid conductivity and permeability even at several kilometers' depth in the crystalline crust (Sausse and Genter 2005; Caspari et al. 2020; Bischoff et al. 2024; Harpers et al. 2024). Steeply dipping strike-slip faults, particularly Set 1, acted as primary conduits for

Fig. 15 Examples of structures controlling the pathways of fluids and the formation of crystalline reservoirs as observed in the field. **a** Steeply dipping fault from the northern part of the batholith. **b** NW-striking strike-slip fault associated with chlorite and epidote precipitation observed at Site 1. **c** Tube-like alterations found at the main NW-striking strike-slip fault mapped at Site 4. **d** Steeply dipping NW-striking strike-slip fault near the southern part of Site 3. **e** Closely spaced NW-striking network of fractures located 500 m east of Site 3

hydrothermal fluids, as indicated by the alignment of alteration zones with subvertical faults, and the observed decrease in alteration intensity with increasing distance from fault cores (Figs. 3, 6, 9, and 10).

Intense mineral alteration at Sites 1 and 4 (Figs. 9, 10, and 15), associated with Stage 1 NW- to WNW-striking faults, provides crucial clues on this fault–alteration relationship. At Site 4 in particular, hydrothermal veins are typically parallel to the main sinistral strike-slip faults formed during Stage 1 (Fig. 10), areas that typically accommodate compressional stress and are not expected to facilitate fluid flow. Conversely, antithetic and extensional fractures associated with the same sinistral strike-slip faults lack veins (Fig. 10a, c), despite the fact that such zones often promote fluid migration and vein precipitation alongside fault activity (Ford et al. 2009). These relationships indicate that vein formation was not coeval with faulting, but instead point to a polyphase brittle deformation–hydrothermal alteration evolution. Supporting evidence comes from the presence of two nearby WNW-striking faults at Site 4, one sinistral and the other dextral, reflecting successive deformation phases (Fig. 10). Collectively, these observations demonstrate that permeability in the Vehmaa Batholith has been primarily controlled by the distribution of post-magmatic brittle structures, which can be further enhanced by mineral alteration over multiple subsequent tectonic and hydrothermal events. Although the precise timing of alteration cannot be constrained from structural data alone, the clear structural control implies that hydrothermal processes postdated Stage 1 faulting, as will be further discussed in the second part of this work.

Geothermal exploration targets

Selecting deep geothermal targets based exclusively on surface mapping presents inherent limitations that constrain accurate resource estimation. These include: (i) uncertainties in fault geometry and their continuity at depth; (ii) the hydraulic behavior of fractures under increasing burial and confining pressure; (iii) the lateral continuity of fracture networks in areas covered by sediments or water; (iv) uncertainty in thermal properties at reservoir depth; (v) lack of in situ stress data, which is critical for assessing fracture dilation tendency and permeability orientation; and (vi) the inability to validate the hydraulic connectivity of lineaments without supporting geophysical and borehole data. To provide a first-order assessment of promising geothermal targets within the Vehmaa Batholith, we identify potential exploration zones based on the following criteria: (i) the extent and continuity of fault zones mapped through lineament analysis; (ii) the presence of fault intersections and terminations indicative of enhanced structural complexity; (iii) fracture connectivity assessed via drone-based photogrammetry; and (iv) the thickness and volume of the plutonic body, which may locally influence the geothermal gradient.

The longest and most continuous lineaments likely represent major kilometer-long fault zones with wide (>200 m) damage zones, which could serve as well-connected fluid pathways, as pointed out by the overall fracture connectivity and intensity approaching 1.7 C_B and 2.0 B_{22}, respectively (Sanderson and Nixon 2018). In particular, the VaFZ, KuFZ, TaFZ and VeFZ (Fig. 16) are identified as large-scale targets that may host kilometer-scale fractured reservoirs, similar in nature to reservoirs utilized by successful projects such as the United Downs Deep Geothermal Project in the UK and geothermal systems in the crystalline basement of the Upper Rhine Graben (Bächler et al. 2003; Ledingham et al. 2019).

Global experience demonstrates that many geothermal reservoirs are not solely linked to individual faults, but are more often associated with structurally complex zones, such as fault intersections, horsetail terminations, relay ramps, step-overs, and accommodation zones, which typically enhance fault permeability and support sustainable fluid flow (e.g., Moeck 2014; Jolie et al. 2021). For example, the VaFZ and KuFZ (Target 1 and 3, Fig. 16), exhibit multiple intersecting structures in their central areas, including a 10-km-long SE-trending lineament and a nearby ENE-trending feature. Additionally, both fault zones are associated with high-density fracture zones (HDFZ; Fig. 12), which together may form localized zones of enhanced permeability. Similarly, the northern part of the TaFZ displays multiple intersections of ENE- and SE-trending lineaments (Target 4, Fig. 16), indicating the potential presence of fractured reservoirs and fluid flow pathways. In contrast, the southern section of the VeFZ is characterized by an anomalously high density of NNW-trending subsidiary lineaments that align with the main fault zone trend (Target 5, Fig. 16), further suggesting large-scale crystalline reservoirs with potential enhanced structural permeability. Additionally, the region between the VaFZ and KuFZ (Target 2, Fig. 16), where two NNW-trending lineaments terminate and appear to connect with SE-trending

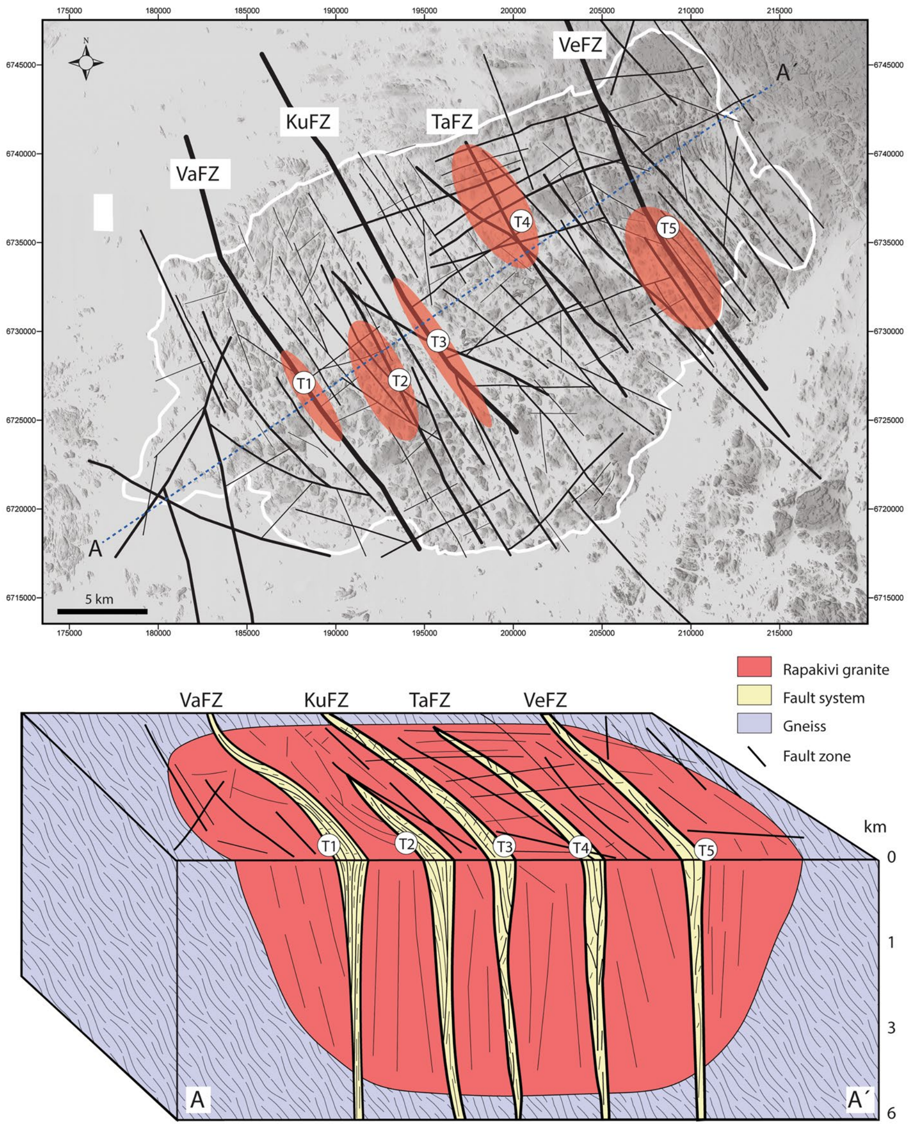

Fig. 16 Schematic representation of prospective targets for geothermal exploration in the Vehmaa Batholith, with favorable locations highlighted in red on the LiDAR map at the top of the figure. Lineaments are mapped on LiDAR-derived topography, with their width scaled to the estimated damage-zone width (1% of lineament length), while major fault zones are deliberately exaggerated to enhance visualization. The figure's vertical dimension is exaggerated by about 3:1 relative to the horizontal

horsetail structures, exhibits increased lineament density, and suggests an extensional geometry that could enhance fracture permeability and fluid flow.

The present-day stress field has not been directly measured within the Vehmaa Batholith. The closest available data come from the Olkiluoto area, located approximately 70 km north of Vehmaa. In Olkiluoto, and more broadly across southern Finland, stress measurements indicate a predominately E–W compressional regime, which contrasts with the NW–SE orientations commonly observed in central Fennoscandia (Heidbach et al. 2025). Although an E–W compressional regime would not enhance dilation along the NNE-trending main structures of Vehmaa, local stress field deviations have been documented in southern Finland. Therefore, for any geothermal

Table 1 Summary of fracture network analysis results from 1:200,000-scale lineaments of Vehmaa Batholith and UAV-derived fracture traces at four study sites

Data	Area (m^2)	Resolution (cm/pixel)	Traces count	Min length (m)	Max length (m)	Mean length (m)	P_{21}	B_{22}	C_B
1:200,000 lineaments	683,476,542	200	137	112.29	18,125.98	5729.02	0.001	1.96	1.69
Site 1	19,269	0.55	86	2.79	91.00	21.84	–	–	–
Site 2	364	0.28	534	0.06	10.65	0.99	1.442	0.69	1.49
Site 3	491	0.28	454	0.095	17.01	1.87	1.724	1.17	1.78
Site 4	610	0.28	2505	0.017	10.92	0.73	2.991	0.76	1.72

The maximum length data are limited by the size of the sampling area and are considered 'minimum' maximum lengths. For lineaments that cross the entire batholith, length is here calculated only for the portion from within the rapakivi. For Site 1, trace statistics are limited due to incomplete exposure, preventing the calculation of derived network metrics. P_{21} = fracture intensity (m/m^2); B_{22} = dimensionless branch intensity; C_B = connections per branch (network connectivity)

project, the prevailing stress conditions should be investigated in detail and at the relevant crustal depths.

The exploration potential of fractured reservoirs in Vehmaa gains further context when compared to regional geothermal conditions. For example, in southern Finland, the geothermal gradient has been defined in detail, with the Metropolitan Helsinki region, approximately 200 km southeast of the study area, showing values of about 17 °C/km and a corresponding heat flow of roughly 52 mW/m^2 (Kukkonen et al. 2023). In Vehmaa, the geothermal gradient is likely controlled by similar geological factors as in other parts of southern Finland and may also be influenced by the total volume of the batholith, which remains poorly constrained. Seismic reflection data and surface mapping indicate that the Wiborg Batholith (Fig. 1) spans approximately 175 km in width and is estimated to be around 30 km thick (Elo and Korja 1993). Assuming the Vehmaa Batholith has a comparable thickness-to-width ratio, its base could extend to depths of around 6–7 km. This estimated depth is supported by seismic reflection data acquired across the northwest margin of the Laitila Batholith, approximately 50 km north of the study area (Fig. 1), where Kukkonen et al. (2010) interpreted the rapakivi granite to occur at depths of at least 4 km. Additionally, rapakivi granite's sheet-like geometry suggests that thickness increases toward the batholith's core (Selonen et al. 2005; Karell et al. 2009), making the central regions particularly relevant for deep geothermal exploration. These geometries of the rapakivi granites and their high concentrations of radioactive elements such as potassium, uranium, and thorium, make them the most heat-producing rocks in southern Finland (Veikkolainen and Kukkonen 2019). Consequently, the Vehmaa area is expected to have a higher geothermal gradient than the surrounding bedrock, and to be similar to the Cornwall region in the UK (Ledingham et al. 2019). In a conservative thermo-hydraulic modeling scenario with a heat flow of 40 mW/m^2, thermal conductivity of 3 W/Km, and a flow rate of 20 L/s, the thermal baseload capacity of a doublet geothermal system exploiting a 100 m wide fault zone at 3 km depth is estimated to average 3 MW_{th} over a 50-year production period (Bischoff et al. 2025).

These hydraulic conditions are likely achievable at such depths in crystalline cratons. For example, calibrated thermal models of the Kola Superdeep Borehole suggest hydraulic permeabilities ranging from 10^{-15} m^2 in the upper 2 km of the crust to 10^{-21} m^2 at

Table 2 Stress tensor parameters derived from the paleostress inversion of fault-slip data

Dataset/stage	n/nt	σ_1 Trend/plunge	σ_2 Trend/plunge	σ_3 Trend/plunge	*R*	*R′*	Stress regime	Tensor type	Quality
All data/Stage 1	36/58	286/06	90/84	196/02	0.42	1.58	Strike-slip	Pure strike-slip	A
All data/Stage 2	16/58	205/02	326/86	115/03	0.37	1.63	Strike-slip	Pure strike-slip	B
High certainty/Stage 1	16/22	291/04	95/86	201/01	0.55	1.45	Strike-slip	Pure strike-slip	B
High certainty/Stage 2	6/22	223/11	344/69	130/17	0.76	1.24	Strike-slip	Transtension	D
High + Moderate/Stage 1	28/46	289/04	103/86	199/00	0.5	1.50	Strike-slip	Pure strike-slip	A
High + Moderate/Stage 2	15/46	216/06	350/81	125/06	0.63	1.37	Strike-slip	Pure strike-slip	B

The number of fault-slip data used versus total measured is represented as n/nt. The principal stress axes are denoted by σ_1, σ_2, σ_3. The stress ratio is defined as R and R′ is the stress regime index as defined in the methods. The stress regime indicates the faulting style based on the orientation of principal stresses. Tensor type refers to the calculated stress regime and corresponding stress geometry. Quality refers to the rating of inversion results, ranging from A (best) to E (worst), according to WinTensor software rating parameters

15 km depth (Kukkonen and Clauser 1994; Mottaghy et al. 2005). At the Kivetty site in Central Finland, a long-term cross-pumping test was conducted to evaluate the hydraulic conductivity of fault-transecting granitic rocks at a depth of 900 m. The test sustained a steady flow of ~0.3 L/s over 27 days, confirming lateral fluid pressure propagation across distances of up to 1.5 km (Carbajal-Martínez et al. 2025). Although the extracted flow was moderate and imposed by the test setup, transmissivity values reached 1.2×10^{-4} m^2 s^{-1}, and laboratory experiments showed that fracture-altered rocks retain high permeability (~10^{-12} m^2) even under confining pressures up to 50 MPa, equivalent to depths of ~2 km (Carbajal-Martínez et al. 2025).

These findings suggest that, under optimized production conditions and with contributions from multiple interconnected fractures, flow rates of 10–30 L/s are feasible in fault-controlled geothermal systems, even within ancient crystalline terrains lacking active tectonics. These observations align with lessons learned from Enhanced Geothermal Systems in analogous crystalline settings, yet higher-temperature settings. For instance, the United Downs Geosystem has demonstrated flow rates exceeding 20 L/s (Reinecker et al. 2021). Likewise, deep geothermal fields in the Upper Rhine Graben have shown that fractured and altered granitic basement can deliver flow rates of up to 60 L/s, enabling production of approximately 1.7 MWe and 24 MWth (Frey et al. 2022).

To confirm the geothermal potential and guide future development of the Vehmaa Batholith and similar crystalline settings, detailed thermo-mechanical-hydraulic (TMH) modeling, supported by deep drilling, is essential. Integrating structural, thermal, rock stress, and hydrological data, together with market trends and a robust policy framework, will be critical for de-risking exploration targets, establishing rapakivi batholiths as a strategic component of Finland's broader geothermal energy roadmap.

Conclusions

This study demonstrates that the brittle structures of the Vehmaa Batholith exhibit a coherent, multiscale pattern, indicative of a cogenetic development of faults and fractures across different scales. The alignment of lineament trends, joint sets, and faults supports a consistent tectonic interpretation, dominated by two major strike-slip faulting phases under WNW–ESE and NNE–SSW compressive-stress regimes. Although some differences exist in paleostress orientations compared to the Åland Rapakivi Batholith, the general structural and tectonic parallels highlight a shared Mesoproterozoic deformation history across southwestern Finland. In the Vehmaa Batholith, structural inheritance plays a central role in the formation of fracture reservoirs in crystalline rocks, with evidence suggesting that alteration zones are controlled by the location of post-magmatic strike-slip faults. The most promising geothermal exploration targets in Vehmaa are associated with the large, subvertical NNW-striking fault system. This system exhibits strong evidence of hydrothermal alteration, elevated fracture intensity, and enhanced secondary porosity—key indicators of effective fluid pathways and reservoir potential. Specific fault zones, such as VaFZ, KuFZ, TaFZ, and VeFZ, likely exhibit the structural complexity, connectivity, and alteration features that are favorable for geothermal development. Zones of intersecting lineaments and horsetail fault geometries are particularly prospective, as they may localize enhanced permeability and promote fluid circulation. Conservative modeling suggests that doublet systems could sustain MW-scale thermal output, supporting the viability of deep geothermal energy development in crystalline settings like Vehmaa. In the second part of this study, we further investigate the processes controlling the formation of crystalline reservoirs, focusing on the role of hydrothermal alteration in enhancing matrix porosity and permeability for sustainable geothermal development in ancient crystalline terrains.

Supplementary Information

The online version contains supplementary material available at https://doi.org/10.1186/s40517-025-00370-5.

Additional file 1

Acknowledgements

This research was funded by the Research Council of Finland under the project "Deep-HEAT-Flows: Discovering deep geothermal resources in low-enthalpy crystalline settings" (Decision No. 354356). Students Marion Spitz, Marianne Leon-Stackow, Hugo Zorninger, and Aurélien Faury from the University of Strasbourg, France, are gratefully acknowledged for their assistance with fieldwork and sample preparation.

Author contributions

NN: conception, fieldwork, analysis and interpretation of data, drafting and revision of the text. AB: conception, fieldwork, analysis and interpretation of data, drafting and revision of the text. DC: fieldwork, analysis and interpretation of data, drafting and revision of the text. JE: fieldwork and revision of the text. KN: fieldwork and revision of the text. PS: analysis and interpretation of data, revision of the text. AN: fieldwork and revision of the text. NO: analysis of data and revision of the text. SB: analysis and interpretation of data, revision of the text. All authors read and approved the manuscript.

Funding

Research Council of Finland, Decision No. 354356.

Data availability

No datasets were generated or analysed during the current study.

Declarations

Competing interests

The authors declare no competing interests.

Received: 27 August 2025 Accepted: 21 November 2025

References

Achtziger-Zupančič P, Loew S, Mariéthoz G. A new global database to improve predictions of permeability distribution in crystalline rocks at site scale. J Geophys Res Solid Earth. 2017;122:3513–39. https://doi.org/10.1002/2017JB014106.

Angelier J. Fault slip analysis and palaeostress reconstruction. Continental Deformation. 1994;4:101–20.

Bächler D, Kohl T, Rybach L. Impact of graben-parallel faults on hydrothermal convection––Rhine Graben case study. Phys Chem Earth a/b/c. 2003;28:431–41. https://doi.org/10.1016/S1474-7065(03)00063-9.

Berger A, Herwegh M. Grain-size-reducing- and mass-gaining processes in different hydrothermal fault rocks. Geol Mag. 2022;159:2219–37. https://doi.org/10.1017/S0016756822000218.

Bergman L, Tynni R, Winterhalter B. Paleozoic sediments in the rapakivi area of the Aland Islands. Geol Survey Finland Bull. 1982;317:7–34.

Bischoff A, Heap MJ, Mikkola P, Kuva J, Reuschlé T, Jolis EM, et al. Hydrothermally altered shear zones: a new reservoir play for the expansion of deep geothermal exploration in crystalline settings. Geothermics. 2024;118:102895. https://doi.org/10.1016/j.geothermics.2023.102895.

Bonnet E, Bour O, Odling NE, Davy P, Main I, Cowie P, et al. Scaling of fracture systems in geological media. Rev Geophys. 2001;39:347–83. https://doi.org/10.1029/1999RG000074.

Bott MHP. The mechanics of oblique slip faulting. Geol Mag. 1959;96:109–17. https://doi.org/10.1017/S0016756800059987.

Carbajal-Martínez D, Wanner C, Diamond LW, Peiffer L, Fletcher JM, Inguaggiato C, et al. Behavior of amagmatic orogenic geothermal systems: insights from the Agua Blanca Fault, Baja California, Mexico. Geochem Geophys Geosyst. 2024;25:e2023GC011145. https://doi.org/10.1029/2023GC011145.

Caspari E, Greenwood A, Baron L, Egli D, Toschini E, Hu K, et al. Characteristics of a fracture network surrounding a hydrothermally altered shear zone from geophysical borehole logs. Solid Earth. 2020;11:829–54. https://doi.org/10.5194/se-11-829-2020.

de Joussineau G. The geometrical properties of fracture corridors. Tectonophysics. 2023;846:229637. https://doi.org/10.1016/j.tecto.2022.229637.

Delvaux D, Sperner B. New aspects of tectonic stress inversion with reference to the TENSOR program. Geological Society, London, Special Publications. 2003;212:75–100. https://doi.org/10.1144/GSL.SP.2003.212.01.06.

Delvaux D, Moeys R, Stapel G, Petit C, Miroshnichenko AI, Ruzhich VV, et al. Paleostress reconstructions and geodynamics of the Baikal region, Central Asia, Part 2. Cenozoic rifting. Tectonophysics. 1997;282:1–38. https://doi.org/10.1016/S0040-1951(97)00210-2.

Diamond LW, Wanner C, Waber HN. Penetration depth of meteoric water in orogenic geothermal systems. Geology. 2018;46:1063–6. https://doi.org/10.1130/G45394.1.

Duwiquet H, Arbaret L, Guillou-Frottier L, Heap MJ, Bellanger M. On the geothermal potential of crustal fault zones: a case study from the Pontgibaud area (French Massif Central, France). Geotherm Energy. 2019;7:33. https://doi.org/10.1186/s40517-019-0150-7.

Duwiquet H, Guillou-Frottier L, Arbaret L, Bellanger M, Guillon T, Heap MJ. Crustal Fault Zones (CFZ) as geothermal power systems: a preliminary 3D THM model constrained by a multidisciplinary approach. Geofluids. 2021;2021:8855632. https://doi.org/10.1155/2021/8855632.

Eklund O, Shebanov AD. The origin of rapakivi texture by sub-isothermal decompression. Precambrian Res. 1999;95:129–46. https://doi.org/10.1016/S0301-9268(98)00130-2.

Elo S, Korja A. Geophysical interpretation of the crustal and upper mantle structure in the Wiborg rapakivi granite area, southeastern Finland. Precambrian Res Baltic Shield. 1993;64:273–88. https://doi.org/10.1016/0301-9268(93)90081-C.

Engström J, Markovaara-Koivisto M, Ovaskainen N, Nordbäck N, Paananen M, Aaltonen I, et al. Mapping of lineaments in Finland at the scale of 1:500 000. Norwegian J Geol. 2025;105:1–9. https://doi.org/10.17850/njg105-1-3.

Evans JP, Forster CB, Goddard JV. Permeability of fault-related rocks, and implications for hydraulic structure of fault zones. J Struct Geol. 1997;19:1393–404. https://doi.org/10.1016/S0191-8141(97)00057-6.

Ford A, Blenkinsop TG, Mclellan JG. Factors affecting fluid flow in strike–slip fault systems: coupled deformation and fluid flow modelling with application to the western Mount Isa Inlier, Australia. Geofluids. 2009;9:2–23. https://doi.org/10.1111/j.1468-8123.2008.00219.x.

Frey M, Bär K, Stober I, Reinecker J, van der Vaart J, Sass I. Assessment of deep geothermal research and development in the Upper Rhine Graben. Geotherm Energy. 2022;10:18. https://doi.org/10.1186/s40517-022-00226-2.

Genter A, Evans K, Cuenot N, Fritsch D, Sanjuan B. Contribution of the exploration of deep crystalline fractured reservoir of Soultz to the knowledge of enhanced geothermal systems (EGS). Comptes Rendus Geoscience, Vers L'exploitation des Ressources Géothermiques Profondes des Systèmes Hydrothermaux Convectifs En Milieux Naturellement Fracturés. 2010;342:502–16. https://doi.org/10.1016/j.crte.2010.01.006.

Glaas C, Vidal J, Genter A. Structural characterization of naturally fractured geothermal reservoirs in the central Upper Rhine Graben. J Struct Geol. 2021;148:104370. https://doi.org/10.1016/j.jsg.2021.104370.

Grasby SE, Hutcheon I. Controls on the distribution of thermal springs in the southern Canadian Cordillera. Can J Earth Sci. 2001;38:427–40. https://doi.org/10.1139/e00-091.

Green PF, Japsen P, Bonow JM, Chalmers JA, Duddy IR, Kukkonen IT. The post-Caledonian thermo-tectonic evolution of Fennoscandia. Gondwana Res. 2022;107:201–34. https://doi.org/10.1016/j.gr.2022.03.007.

Haapala I. Petrography and geochemistry of the Eurajoki stock, a rapakivi-granite complex with greisen-type mineralization in southwestern Finland. Bull Geol Survey Finland. 1997;286:1–98.

Harpers N, Forbes Inskip N, Allen MJ, Buckman J, Faulkner DR, Claes H, et al. Effects of chemical alteration on frictional properties in a deep, granitic, geothermal system in Cornwall: direct shear experiments at near in situ conditions. J Geophys Res Solid Earth. 2024;129:e2024JB028861. https://doi.org/10.1029/2024JB028861.

Hautaniemi H, Kurimo M, Multala J, Leväniemi H, Vironmäki J. The "Three in One" Aerogeophysical Concept of Gtk in 2004. Geol Surv Finland Spec Pap. 2005;39(21–74):2005.

Jolie E, Scott S, Faulds J, Chambefort I, Axelsson G, Gutiérrez-Negrín LC, et al. Geological controls on geothermal resources for power generation. Nature Reviews Earth & Environment. 2021;2:324–39. https://doi.org/10.1038/s43017-021-00154-y.

Karell F, Ehlers C, Airo M-L, Selonen O. Intrusion mechanisms and magnetic fabrics of the Vehmaa rapakivi granite batholith in SW Finland. Geotectonics. 2009;96:53–68. https://doi.org/10.1127/1864-5658/09/96-0053.

Korja A, Korja T, Luosto U, Heikkinen P. Seismic and geoelectric evidence for collisional and extensional events in the Fennoscandian Shield implications for Precambrian crustal evolution. Tectonophysics, Plate Tectonic Signatures in the Continental Lithosphere. 1993;219:129–52. https://doi.org/10.1016/0040-1951(93)90292-R.

Kraal KO, Ayling BF, Blake K, Hackett L, Perdana TSP, Stacey R. Linkages between hydrothermal alteration, natural fractures, and permeability: integration of borehole data for reservoir characterization at the Fallon FORGE EGS site, Nevada, USA. Geothermics. 2021;89:101946. https://doi.org/10.1016/j.geothermics.2020.101946.

Kukkonen IT, Clauser C. Simulation of heat transfer at the Kola deep-hole site: implications for advection, heat refraction and palaeoclimatic effects. Geophys J Int. 1994;116:409–20. https://doi.org/10.1111/j.1365-246X.1994.tb01806.x.

Kukkonen IT, Heikkinen PJ, Malin PE, Renner J, Dresen G, Karjalainen A, et al. Hydraulic conductivity of the crystalline crust: insights from hydraulic stimulation and induced seismicity of an enhanced geothermal system pilot reservoir at 6 km depth, Espoo, southern Finland. Geothermics. 2023;112:102743. https://doi.org/10.1016/j.geothermics.2023.102743.

Kukkonen IT, Kohn B, Kirsimäe K, Jõeleht A, Chung L, McMillan M, et al. Phanerozoic evolution of Fennoscandia: Evidence from apatite fission track, fluid flow and geodynamic data in Finland and Estonia. Gondwana Res. 2025. https://doi.org/10.1016/j.gr.2025.04.004.

Lacombe O. Do fault slip data inversions actually yield "paleostresses" that can be compared with contemporary stresses? A critical discussion. Comptes Rendus - Geoscience. 2012;344:159–73. https://doi.org/10.1016/j.crte.2012.01.006.

Lahtinen R, Korja A, Nironen M, Heikkinen P. Palaeoproterozoic accretionary processes in Fennoscandia. Geological Society, London, Special Publications. 2009;318:237–56. https://doi.org/10.1144/SP318.8.

Ledésert B, Hebert R, Genter A, Bartier D, Clauer N, Grall C. Fractures, hydrothermal alterations and permeability in the Soultz Enhanced Geothermal System. Comptes Rendus Geoscience, Vers L'exploitation des Ressources Géothermiques Profondes des Systèmes Hydrothermaux Convectifs En Milieux Naturellement Fracturés. 2010;342:607–15. https://doi.org/10.1016/j.crte.2009.09.011.

Li A-B, Xu S-Y, Liu X-Y, Lü G-N, Xie X-L, Fox M. Relative dating of fault activity using the principle of cross-cutting relationships: an automated approach. Comput Geosci. 2024;192:105702. https://doi.org/10.1016/j.cageo.2024.105702.

Manzocchi T. The connectivity of two-dimensional networks of spatially correlated fractures. Water Resour Res. 2002;38:1-1-1–20. https://doi.org/10.1029/2000WR000180.

Marchesini B, Garofalo PS, Menegon L, Mattila J, Viola G. Fluid-mediated, brittle–ductile deformation at seismogenic depth – part 1: fluid record and deformation history of fault veins in a nuclear waste repository (Olkiluoto Island, Finland). Solid Earth. 2019;10:809–38. https://doi.org/10.5194/se-10-809-2019.

Martel SJ. Progress in understanding sheeting joints over the past two centuries. J Struct Geol. 2017;94:68–86. https://doi.org/10.1016/j.jsg.2016.11.003.

Mattila J, Viola G. New constraints on 1.7 Gyr of brittle tectonic evolution in southwestern Finland derived from a structural study at the site of a potential nuclear waste repository (Olkiluoto Island). J Struct Geol. 2014;67:50–74. https://doi.org/10.1016/j.jsg.2014.07.003.

Mattsson T, McCarthy W, Schmiedel T. Transport of magma in granitic mush systems; an example from the Götemar pluton, Sweden. Geochem Geophys Geosyst. 2024;25:e2023GC011061. https://doi.org/10.1029/2023GC011061.

Mitchell TM, Faulkner DR. The nature and origin of off-fault damage surrounding strike-slip fault zones with a wide range of displacements: a field study from the Atacama fault system, northern Chile. J Struct Geol. 2009;31:802–16. https://doi.org/10.1016/j.jsg.2009.05.002.

Moeck IS. Catalog of geothermal play types based on geologic controls. Renew Sustain Energy Rev. 2014;37:867–82. https://doi.org/10.1016/j.rser.2014.05.032.

Mottaghy D, Schellschmidt R, Popov YA, Clauser C, Kukkonen IT, Nover G, et al. New heat flow data from the immediate vicinity of the Kola super-deep borehole: vertical variation in heat flow confirmed and attributed to advection. Tectonophysics. 2005;401:119–42. https://doi.org/10.1016/j.tecto.2005.03.005.

Nironen M. The Svecofennian orogen: a tectonic model. Precambrian Res. 1997;86:21–44. https://doi.org/10.1016/S0301-9268(97)00039-9.

Nordbäck N, Mattila J, Zwingmann H, Viola G. Precambrian fault reactivation revealed by structural and K-Ar geochronological data from the spent nuclear fuel repository in Olkiluoto, southwestern Finland. Tectonophysics. 2022;824:229208. https://doi.org/10.1016/j.tecto.2022.229208.

Nordbäck N, Skyttä P, Engström J, Ovaskainen N, Mattila J, Aaltonen I. Mesoproterozoic strike-slip faulting within the Åland Rapakivi Batholith, Southwestern Finland. Τeκтonika. 2024;2:1–26. https://doi.org/10.55575/tektonika2024.2.1.51.

Nyberg B, Nixon CW, Sanderson DJ. NetworkGT: a GIS tool for geometric and topological analysis of two-dimensional fracture networks. Geosphere. 2018;14:1618–34. https://doi.org/10.1130/GES01595.1.

Ovaskainen N. fractopo: a Python package for fracture network analysis. J Open Source Softw. 2023;8:5300. https://doi.org/10.21105/joss.05300.

Ovaskainen N, Nordbäck N, Skyttä P, Engström J. A new subsampling methodology to optimize the characterization of two-dimensional bedrock fracture networks. J Struct Geol. 2022;155:104528. https://doi.org/10.1016/j.jsg.2022.104528.

Ovaskainen N, Skyttä P, Nordbäck N, Engström J. Detailed investigation of multi-scale fracture networks in glacially abraded crystalline bedrock at Åland Islands, Finland. Solid Earth. 2023;14:603–24. https://doi.org/10.5194/se-14-603-2023.

Pascal C. Paleostress inversion techniques - 1st edition. Elsevier; 2021.

Peacock DCP, Sanderson DJ. Structural analyses and fracture network characterisation: seven pillars of wisdom. Earth Sci Rev. 2018;184:13–28. https://doi.org/10.1016/j.earscirev.2018.06.006.

Peacock DCP, Nixon CW, Rotevatn A, Sanderson DJ, Zuluaga LF. Glossary of fault and other fracture networks. J Struct Geol. 2016;92:12–29. https://doi.org/10.1016/j.jsg.2016.09.008.

Peacock DCP, Nixon CW, Rotevatn A, Sanderson DJ, Zuluaga LF. Interacting faults. J Struct Geol. 2017;97:1–22. https://doi.org/10.1016/j.jsg.2017.02.008.

Penhoët E, Arbaret L, Guillou-Frottier L, Duwiquet H, Gumiaux C, Bellanger M. Fluid flow in crustal fault zones with varying lengthwise thickness: application to the Margeride fault zone (French Massif Central). Geotherm Energy. 2025;13:6. https://doi.org/10.1186/s40517-025-00334-9.

Pokki J, Kohonen J, Lahtinen R, Rämö TO, Andersen T. Petrology and provenance of the Mesoproterozoic Satakunta formation, SW Finland. Espoo: Geological Survey of Finland; 2013.

Prando F, Menegon L, Anderson M, Marchesini B, Mattila J, Viola G. Fluid-mediated, brittle–ductile deformation at seismogenic depth – part 2: stress history and fluid pressure variations in a shear zone in a nuclear waste repository (Olkiluoto Island, Finland). Solid Earth. 2020;11:489–511. https://doi.org/10.5194/se-11-489-2020.

Questiaux J-M, Couples GD, Ruby N. Fractured reservoirs with fracture corridors. Geophys Prospect. 2010;58:279–95. https://doi.org/10.1111/j.1365-2478.2009.00810.x.

Rämö OT, Haapala I. One hundred years of rapakivi granite. Mineral Petrol. 1995;52:129–85. https://doi.org/10.1007/BF01163243.

Reinecker J, Gutmanis J, Foxford A, Cotton L, Dalby C, Law R. Geothermal exploration and reservoir modelling of the United Downs deep geothermal project, Cornwall (UK). Geothermics. 2021;97:102226. https://doi.org/10.1016/j.geothermics.2021.102226.

Saintot A, Stephens MB, Viola G. Brittle tectonic evolution and paleostress field reconstruction in the southwestern part of the Fennoscandian Shield, Forsmark, Sweden. Tectonics. 2011;30:1–36. https://doi.org/10.1029/2010TC002781.

Sanderson DJ, Nixon CW. The use of topology in fracture network characterization. J Struct Geol. 2015;72:55–66. https://doi.org/10.1016/j.jsg.2015.01.005.

Sanderson DJ, Nixon CW. Topology, connectivity and percolation in fracture networks. J Struct Geol. 2018;115:167–77. https://doi.org/10.1016/j.jsg.2018.07.011.

Sanderson DJ, Peacock DCP. Line sampling of fracture swarms and corridors. J Struct Geol. 2019;122:27–37. https://doi.org/10.1016/j.jsg.2019.02.006.

Sanderson DJ, Peacock DCP. Making rose diagrams fit-for-purpose. Earth-Sci Rev. 2020;201:103055. https://doi.org/10.1016/j.earscirev.2019.103055.

Sausse J, Genter A. Types of permeable fractures in granite. Geological Society, London, Special Publications. 2005;240:1–14. https://doi.org/10.1144/GSL.SP.2005.240.01.01.

Scherneck H-G, Lidberg M, Haas R, Johansson JM, Milne GA. Fennoscandian strain rates from BIFROST GPS: a gravitating, thick-plate approach. J Geodyn. 2010;50:19–26. https://doi.org/10.1016/j.jog.2009.11.005.

Scholz CH, Dawers NH, Yu J-Z, Anders MH, Cowie PA. Fault growth and fault scaling laws: preliminary results. J Geophys Res Solid Earth. 1993;98:21951–61. https://doi.org/10.1029/93JB01008.

Selonen O, Ehlers C, Luodes H, Lerssi J. The vehmaa rapakivi granite batholith - an assemblage of successive intrusions indicating a piston-type collapsing centre. Bull Geol Soc Finl. 2005;77:65–70. https://doi.org/10.17741/bgsf/77.1.004.

Sibson RH. Structural permeability of fluid-driven fault-fracture meshes. J Struct Geol. 1996;18:1031–42. https://doi.org/10.1016/0191-8141(96)00032-6.

Siler DL, Faulds JE, Hinz NH, Dering GM, Edwards JH, Mayhew B. Three-dimensional geologic mapping to assess geothermal potential: examples from Nevada and Oregon. Geotherm Energy. 2019;7:2. https://doi.org/10.1186/s40517-018-0117-0.

Simonen A. The precambrian in Finland. Espoo: Geologinen tutkimuslaitos; 1980.

Skyttä P, Ovaskainen N, Nordbäck N, Engström J, Mattila J. Fault-induced mechanical anisotropy and its effects on fracture patterns in crystalline rocks. J Struct Geol. 2021;146:104304. https://doi.org/10.1016/j.jsg.2021.104304.

Stober I, Zhong J, Zhang L, Bucher K. Deep hydrothermal fluid–rock interaction: the thermal springs of Da Qaidam, China. Geofluids. 2016;16:711–28. https://doi.org/10.1111/gfl.12190.

Suominen V. The chronostratigraphy of southwestern Finland: with special reference to Postjotnian and Subjotnian diabases, Geological Survey of Finland bulletin. Espoo: Geologian Tutkimuskeskus; 1991.

Taillefer A, Guillou-Frottier L, Soliva R, Magri F, Lopez S, Courrioux G, et al. Topographic and faults control of hydrothermal circulation along dormant faults in an orogen. Geochem Geophys Geosyst. 2018;19:4972–95. https://doi.org/10.1029/2018GC007965.

Tchalenko JS. Similarities between shear zones of different magnitudes. GSA Bull. 1970;81:1625–40. https://doi.org/10.1130/0016-7606(1970)81[1625:SBSZOD]2.0.CO;2.

Torvela T, Ehlers C. From ductile to brittle deformation: structural development and strain distribution along a crustal-scale shear zone in SW Finland. Int J Earth Sci. 2010;99:1133–52. https://doi.org/10.1007/s00531-009-0451-3.

Torvela T, Mänttäri I, Hermansson T. Timing of deformation phases within the South Finland shear zone, SW Finland. Precambrian Res. 2008;160:277–98. https://doi.org/10.1016/j.precamres.2007.08.002.

Tynni R. On paleozoic microfossils in clastic dykes on the Åland Islands and in the core samples of Lumparn. Geol Survey Finland Bull. 1982;317:35–94.

Uski M, Oinonen K, Lund B, Soosalu H, Ottemöller L, Sørensen MB, et al. FENCAT—an update of the Fennoscandian earthquake catalogue. Geophys J Int. 2025;242(3):ggaf242. https://doi.org/10.1093/gji/ggaf242.

Väisänen M, Skyttä P. Late Svecofennian shear zones in southwestern Finland. GFF. 2007;129:55–64. https://doi.org/10.1080/11035890701291055.

Veikkolainen T, Kukkonen IT. Highly varying radiogenic heat production in Finland, Fennoscandian Shield. Tectonophysics. 2019;750:93–116. https://doi.org/10.1016/j.tecto.2018.11.006.

Vermilye JM, Scholz CH. The process zone: a microstructural view of fault growth. J Geophys Res Solid Earth. 1998;103:12223–37. https://doi.org/10.1029/98JB00957.

Wallace RE. Geometry of shearing stress and relation to faulting. J Geol. 1951;59:118–30. https://doi.org/10.1086/625831.

Whipp DM Jr., Ehlers TA. Influence of groundwater flow on thermochronometer-derived exhumation rates in the central Nepalese Himalaya. Geology. 2007;35:851–4. https://doi.org/10.1130/G23788A.1.

Zhang Q, Dahi Taleghani A. Autonomous fracture flow tuning to enhance efficiency of fractured geothermal systems. Energy. 2023;281:128163. https://doi.org/10.1016/j.energy.2023.128163.

Arola T, Wiberg M. Geothermal Energy Use, Country Update for Finland, European Geothermal Congress 2022, Berlin. https://www.fu-confirm.de/assets/country_updates_EGC2022.pdf. Accessed 5 June 2025.

Bhattacharya AR. Strike-slip faults. In: Bhattacharya AR, editor. Structural Geology. Cham: Springer International Publishing; 2022. https://doi.org/10.1007/978-3-030-80795-5_12

Bischoff A, Carbajal-Martínez D, Heap MJ, Reuschlé T, Kuva J, Jolis EM, Cutts K, Piipponen K. 2025. Crystal Clear: A Petrophysical Databank of Crystalline Rocks for Assessing Deep Geothermal Reservoirs in Fault Zones. Presented at the European Geothermal Congress 2025, Zurich, Switzerland. https://media.voog.com/0000/0050/7355/files/Bischoff_et_al_2025_crystal_clear_FINAL.pdf. Accessed 9 June 2025.

Carbajal-Martínez D, Bischoff A, Heap MJ, Jolis EM, Reuschlé T, Luoto T, Kuva J, Vuoriainen S, Engström J, Kortunov E, Nordbäck N. From Faults to Flow: How Fracturing and Hydrothermal Alteration Shape Geothermal Reservoirs in Crystalline Rocks. Presented at the European Geothermal Congress 2025, Zurich, Switzerland. 2025. https://media.voog.com/0000/0050/7355/files/EGC2025_Carbajal-Martinez_Kivetty_Paper.pdf. Accessed 9 June 2025. https://doi.org/10.1016/j.renene.2020.12.113.

EMODnet Bathymetry Consortium. 2018. EMODnet Digital Bathymetry (DTM 2018). https://doi.org/10.12770/18FF0D48-B203-4A65-94A9-5FD8B0EC35F6.

Farndale H, Law R. An Update on the United Downs Geothermal Power Project, Cornwall, UK. 2022. In: Proceedings, 47th Workshop on Geothermal Reservoir Engineering Stanford University, Stanford, California, 7–9 Feb 2022.

GTK. Geological map of the Fennoscandian shield 1:1 000 000. Hakku, 2001. https://hakku.gtk.fi/en/locations/search.

GTK. Aeromagnetic raster data of Finland, Hakku. 2007a. https://hakku.gtk.fi/en/locations/search.

GTK. Aeroelectromagnetic raster data of Finland, Hakku. 2007b. https://hakku.gtk.fi/en/locations/search.

Heidbach O, Rajabi M, Di Giacomo D, Harris J, Lammers S, Morawietz S, Pierdominici S, Reiter K, von Specht S, Storchak D, Ziegler MO. World Stress Map Database Release 2025. GFZ Data Services. 2025. https://doi.org/10.5880/WSM.2025.001.

IEA. 2024. The Future of Geothermal Energy, IEA, Paris. 2024. https://www.iea.org/reports/the-future-of-geothermal-energy. Accessed 5 June 2025.

IRENA. 2022. Renewable power generation costs in 2022, International Renewable Energy Agency, Abu Dhabi. 2022. https://www.connaissancedesenergies.org/sites/connaissancedesenergies.org/files/pdf-pt-vue/IRENA_Renewable_power_generation_costs_in_2022.pdf. Accessed 5 June 2025.

Kohonen J, Pihlaja P, Kujala H, Marmo J. Sedimentation of the Jotnian Satakunta sandstone, western Finland. J Geol Soc Finland 1993; 369.

Kukkonen I, Paananen M, Elo S, Paulamäki S, Laitinen J. HIRE Seismic Reflection Survey in the Olkiluoto Area. Working report by HIRE Working group of the Geological Survey of Finland. Heikkinen, P., Heinonen, S from Institute of Seismology, University of Helsinki. Posiva Oy in co-operation. 2010.

Ledingham P, Cotton L, Law R. The United Downs Deep Geothermal Power project. 2019. In: Proceedings of the European Geothermal Congress. Presented at the 44th Workshop on Geothermal Reservoir Engineering 2019, Stanford, California.

Lindberg B, Bergman L. Vehmaa. Explanation to the Geological map of Finland 1:100 000, pre-Quaternary rocks, sheet 1042. 1993. p. 1–56. Geological Survey of Finland (In Finnish with English summary).

National Land Survey of Finland. Laser scanning 2008–2019 by National Land Survey of Finland. 2019. https://www.maanmittauslaitos.fi/en/maps-and-spatial-data/expert-users/product-descriptions/laser-scanning-data.

Nordbäck N, Ovaskainen N, Markovaara-Koivisto M, Skyttä P, Ojala A, Nixon C. Multiscale mapping and scaling analysis of the censored brittle structural framework within the crystalline bedrock of southern Finland. Bull Geol Soc Finland 95. 2023. https://doi.org/10.17741/bgsf/95.1.001

Pollard DD, Segall P. Theoretical displacements and stresses near fractures IN rock: with applications to faults, joints, veins, dikes, and solution surfaces. In: Atkinson BK, editor. Fracture mechanics of rock. London: Academic Press; 1987. p. 277–349. https://doi.org/10.1016/B978-0-12-066266-1.50013-2

Rämö OT, Haapala I. Chapter 12 Rapakivi Granites. In: Lehtinen M, Nurmi PA, Rämö OT, editors. Developments in precambrian geology, precambrian geology of Finland key to the evolution of the Fennoscandian shield. Amsterdam: Elsevier; 2005. p. 533–562. https://doi.org/10.1016/S0166-2635(05)80013-1

Sanner B, Antics M, Baresi M, Urchueguia J, Dumas P. Summary of EGC 2022 Country Update Reports on Geothermal Energy in Europe, European Geothermal Congress 2022, Berlin, https://www.fu-confirm.de/assets/country_updates_EGC2022.pdf. 2022. Accessed 5 June 2025.

Scholz CH. 6.10 - Fault mechanics. In: Schubert G, editor. Treatise on Geophysics. Amsterdam: Elsevier; 2007. p. 441–483. https://doi.org/10.1016/B978-044452748-6.00111-5

Viola G, Mattila J, Zwingmann H, Todd A, Raven M. Structural and K/Ar Illite geochronological constraints on the brittle deformation history of the Olkiluoto Region, Southwest Finland. Posiva Working Report. 2011. Posiva Oy, Eurajoki.

Publisher's Note